Microstructure-property correlations in as-built and heat-treated compositionally graded stainless steel 316L-Inconel 718 alloy fabricated by laser powder bed fusion

Yaojie Wen [a b], Jianbao Gao [c], Ramasubramanian Lakshmi Narayan [d], Pei Wang [e], Lijun Zhang [c], Baicheng Zhang [a b], Upadrasta Ramamurty [e f], Xuanhui Qu [a b]

[a] Beijing Advanced Innovation Center Materials Genome Engineering, Advanced Material & Technology Institute, University of Science and Technology Beijing, Beijing, 100083, China

[b] Beijing Laboratory of Metallic Materials and Processing for Modern Transportation, Beijing, 100083, China

[c] State Key Laboratory of Powder Metallurgy, Central South University, Changsha, 410083, Hunan, PR China

[d] Department of Materials Science and Engineering, Indian Institute of Technology, Delhi, Hauz Khas, New Delhi, 110016, India

[e] IMRE - Institute of Materials Research and Engineering, 2 Fusionopolis Way, Innovis, #08-03, 138634, Singapore

[f] School of Mechanical & Aerospace Engineering, Nanyang Technological University, Singapore

Abstract

The microstructures and the mechanical properties of a laser powder bed fusion manufactured compositionally graded alloy of the austenitic stainless steel 316L and Inconel 718, in the as-built and heat-treated conditions, were investigated. In all the cross sections of the as-built compositionally graded alloy, along the compositional gradient direction, which is perpendicular to the build direction, the microstructure primarily consists of sub-micron sized cells embedded within <001> textured columnar grains of the γ phase along with Laves phases at their grain boundaries. Heat treatment, which involves solutionizing at 1040 °C for 1 h followed by annealing at 720 °C and 620 °C for 10 h each, leads to coarsening of Laves phases, slight modification in texture and the annihilation of the sub-grain structure of the compositionally graded alloy, but does not alter the columnar grain size. It also leads to precipitation of the γ" and γ' phases in the portions of the compositionally graded alloy with >70 wt% of IN718. The

hardness, yield strength and tensile strength of the compositionally graded alloy increase but ductility decreases from the SS316L-rich end to the IN718-rich end along the gradient direction. Heat treatment smoothens the variations in YS and UTS along the gradient direction in cross sections with <82 wt% IN718 but reduces their relative magnitude compared to that of the as-built condition. The heat-treated compositionally graded alloy exhibits significantly higher YS and UTS but lower ductility than that in the as-built condition, in portions with ≥82 wt% IN718. These mechanical property variations are analyzed in detail by considering variations in the composition, microstructural features, and contents of different phases in the as-built and heat-treated compositionally graded alloy. Finally, an appraisal on the appropriate compositional gradient and utility of the heat treatment of the compositionally graded alloy is discussed in the context of specific requirements in structural applications.

Keywords

Laser powder bed fusion; Compositionally graded alloys; Superalloy; Steel; Mechanical behavior

1. Introduction

The austenitic stainless steel 316L (SS316L) and Inconel 718 (IN718) are traditionally joined together by arc or electron beam welding for fabricating compressor rotors in gas and steam turbine engines [[1], [2], [3]]. However, reports suggest that during welding, the heat affected zone in these joints undergoes liquation or solidification cracking [4]. Moreover, to improve the mechanical properties of the IN718 component, a double ageing heat treatment is performed on the component, where it is solutionized above 1100 °C for 1 h and subsequently aged at 720 and 620 °C for 10 h each [5]. While this heat treatment leads to the nucleation and coarsening of the coherent γ" and γ' precipitates in IN718, which improve its strength significantly, it also promotes the formation of several brittle intermetallic phases at the weld joint of IN718 and SS316L. These intermetallic phases act as crack initiators during high temperature service as the weld joints develop strain incompatibilities due to the difference in the coefficients of thermal expansion of the two alloys [6].

To alleviate these problems, a strategy of introducing a composition gradient, i.e., varying the relative proportions of SS316L and IN718 continuously along a specific dimension, is considered. In the produced compositionally graded alloy (CGA) of SS316L and IN718, the discontinuity in composition is smoothened out. Simultaneously, this also introduces a gradient in the microstructure and thermal expansion coefficient of the CGA, which prevents the build-up of stresses at any location and prevents cracking during elevated temperature service [7,8]. CGAs are traditionally fabricated by chemical or physical vapor deposition (CVD/PVD), thermal spraying, powder sintering, centrifugal casting, and self-propagating high temperature synthesis (SHS). However, in most of these methods, there is limited control over the geometry, density and composition of the fabricated component. In this context, additive manufacturing (AM) is an attractive alternative to fabricate CGAs as it enables customizability in terms of the geometric design, dimensional accuracy and compositional variations [[9], [10], [11], [12]]. Moreover, components built by AM have a low 'buy-to-fly' ratio as AM only utilizes the requisite amount of raw material for building the component. This reduces the cost of manufacturing significantly in addition to minimizing material wastage. Of the various AM techniques that are being pursued actively, laser powder bed fusion (LPBF) and laser directed energy deposition (LDED) have hitherto been employed to fabricate CGAs of SS316L and IN718 [[13], [14], [15], [16], [17], [18], [19], [20]]. In most of these studies, the CGA is built vertically, whereby the composition gradient is aligned along the build direction. It was observed that CGAs produced in this fashion were either of poor quality, in terms of the smoothness in compositional gradient [17], or had cracks in them [14,19].

As an alternative, we recently devised a novel powder dispensing strategy, which introduces composition gradient in the plane of the powder bed (i.e., perpendicular to the build direction). Using this method, a crack-free and highly dense CoCrMo/IN718 CGA, which has a smooth compositional gradient, was produced [21]. In this paper, we present a study on the fabrication of a similar high quality SS316L/IN718 CGA using the above-mentioned method. First, the process parameters for printing the CGA were optimized in terms of minimizing the porosity of the build. This was followed by a thorough composition, microstructural, and mechanical characterization of different

cross sections in the CGA. A double ageing heat treatment was also performed on the as-built CGA and the resulting microstructure and mechanical properties were examined and compared with those of the as-built condition. Complementary CALPHAD (Calculation of Phase Diagrams) simulations were performed to understand the evolution of the Laves phases during the heat treatment. The experimental results of this study show that the LPBF method used in our study is capable of fabricating high density, crack-free SS316L/IN718 CGAs that have a smooth composition gradient along the length. Finally, structure-mechanical property correlations and deformation mechanisms in each cross section of the as-built and heat-treated CGA were discussed with the aim of providing insights on its expected structural performance. On the basis of these analyses, application specific pointers on the appropriate compositional gradients and heat treatment are provided.

2. Experimental methods

2.1. Powder dispensing system and CGA printing by LPBF

A custom designed continuous gradient powder feeding device integrated with a commercial LPBF system was used in this study. This device mixes two powders homogeneously in the desired proportions and creates a composition gradient along the powder bed plane (perpendicular to the build direction). The schematic of the system is shown in Fig. 1 (a) and other details regarding its functioning are provided in our previous work [21]. The LPBF system is equipped with a 500 W fiber laser which has a wavelength of 1070 nm and spot size (diameter) of 35 μm. Printing is performed in an argon atmosphere.

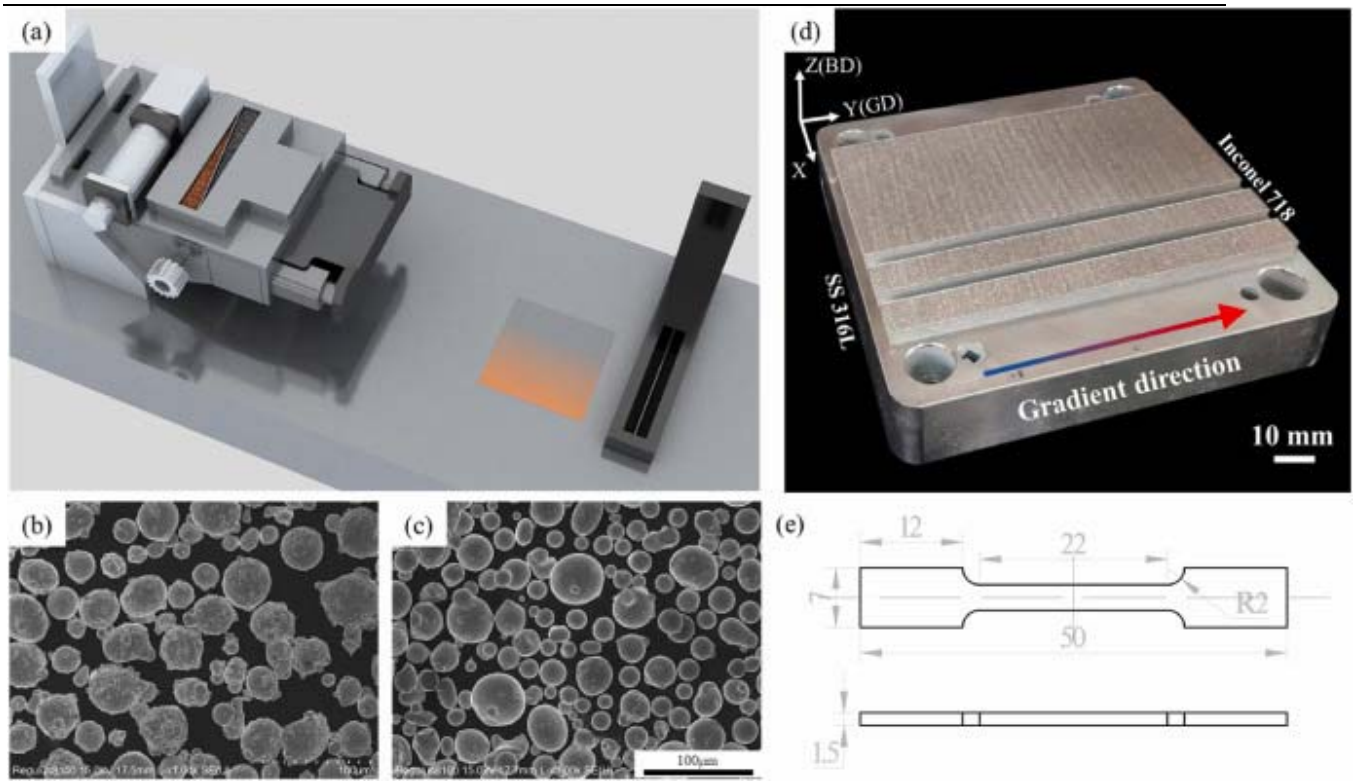

1. Download: Download high-res image (872KB)
2. Download: Download full-size image

Fig. 1. (a) Schematic illustration of the CGA LPBF system; (b) and (c) SEM images of the powders of two alloys, SS316L and IN718; (d) Photographing image of the SS316L-IN718 CGA samples; (e) Geometry of the tensile test coupons.

Powders of SS316L and IN718 were selected for preparing the CGA. The two powders were first loaded in the dual chamber powder hopper that has a diagonal separator. From this hopper, the powders move to a powder mixer that maintains the desired gradient in composition when the powders are spread over the printing substrate. Finally, the recoater spreads the mixed powders on the platform and scanned by the laser to fabricate a build. In Fig. 1(d), images of two CGA builds, with sizes,

50 × 110 × 6 mm^3 and 10 × 110 × 6 mm^3 (X × Y × Z), are displayed. Labels indicating the alloy composition and gradient direction (GD) are marked on the sample. Post building, one CGA build was subjected first to a homogenizing treatment, wherein it is heated to 1040 °C for 1 h followed by air cooling to room temperature (RT). Then it is subjected to a two-stage ageing treatment, where it is heated to 720 °C and 620 °C for 10 h each and then air cooled to RT. Other details of this double ageing (DA) heat treatment can be found in the reference [5]. The other build is only subjected to a stress relief treatment and is therefore considered as the as-built condition.

2.2. Feedstock powder materials

Gas atomized spherical SS316L and IN718 powders with particle size distribution that ranges between 15 and 53 μm were used in this study. Table 1 lists the chemical compositions of the SS316L and IN718 powders, while their particle morphologies are displayed in Fig. 1 (b) and (c), respectively.

Table 1. Chemical compositions of the SS316L and IN718 powders (in wt. %).

SS 316L	Fe	Cr	Ni	Mn	Mo	O	Si	C
	Bal.	16.8	12.1	1.87	2.25	0.12	0.03	0.02
IN 718	Ni	Fe	Cr	Nb	Mo	Ti	Al	O
	Bal.	19.75	19.92	4.97	2.92	0.77	0.39	0.0186

2.3. Characterization methods

For metallographic investigations, different cross-section slices of the CGA builds along the GD were cut, polished and prepared according to the ASTM E3-11 standard [22]. The Archimedes method for measuring the relative density cannot be used as the theoretical density in each section is not known *a priori*. Therefore, porosity volume fraction was measured on each cross-section using optical microscopy (OM, ZEISS AXIO) and estimated with the ImageJ software.

Chemical compositions of the builds were measured by energy dispersive spectroscopy (EDS, Bruker) and X-ray fluorescence spectrometry (XRF, Bruker M4 Tornado). EDS analysis was conducted on 65 locations along GD at an interval of 1.5 mm; 3 measurements were made at each location. The cross-section slices cut along GD in both CGA builds were etched with 0.5 g $CuCl_2$ + 10 ml C_2H_5OH + 10 ml HCl for 20–40 s before observing them with a scanning electron microscope (SEM, Hitachi FE-SEM SU8100). The samples were polished on Vibratory Polisher with silica suspension for 6h for Electron backscatter diffraction (EBSD, HKL Nordlysnano). EBSD was conducted to obtain the crystallographic information of grains with a step size of 0.5 μm and the area of each figure is 500*500 μm. The phase analysis was investigated using X-ray Diffraction (XRD, Rigaku Ultima-IV) with Cu Kα radiation. Transmission electron microscopy (TEM, FEI TECNAI G2 F20) was used to determine the crystal structures and compositions of phases and precipitates.

Vickers microhardness along GD was measured with a load of 200 g and a dwell time of 10 s. Tensile test coupons of different compositions were cut at equal intervals from each end from the 50 × 110 × 6 mm^3 CGA builds. The loading axis of each tensile specimen was oriented parallel to GD. Quasistatic tensile tests were performed at room temperature on a CMT4105 universal testing machine with a cross-head displacement rate of 1 mm/min. The loading axis was normal to the gradient direction and build direction. Three tests were performed for each composition to ensure repeatability of results.

2.4. Phase evolution analysis

The Thermo-Calc software was used for the predicting the evolution of phases along GD in the as-built SS316L/IN718 CGA [23]. The thermodynamic databases TCFE8, TCNI9 were used to study the SS316L and IN718 components of CGA [24]. The Scheil solidification module in Thermo-Calc was used to predict the phase composition of the CGA under the non-equilibrium solidification conditions. To accelerate the computation speed of the Scheil simulations, the recently developed high-throughput computation platform, Malac-Distmas [25], was utilized.

3. Results

3.1. Laser parameter optimization for LPBF fabrication of SS316L/IN718 CGA

The alloys SS316L and IN718 have different melting points and solidification characteristics, which means that the optimal laser processing parameters, i.e., laser power and scan speed, for their individual fabrication will also be different. Therefore, fabricating a mixture of these two alloys requires a different strategy for process parameter optimization. One possible strategy for determining the ideal process parameter for the alloy mixture is to find an overlap in the individual process parameter sets of both alloys after fixing other processing parameters, such as layer thickness and the hatch distance. For this study, these were chosen as ~40 and ~90 μm, respectively. Fig. 2 (a) and (b) displays the process parameter map of laser power and scan velocity for SS316L and IN718, respectively. In these maps, the color of each data point represents the relative density of the build obtained by employing different combinations of laser power and scan velocity. The color scale is provided alongside the process parameter maps in Fig. 2. A benchmark of relative density >99% is set to determine the optimal process parameters for individual builds. From these maps, the only optimal laser power and scan velocity parameter set that is common to both alloys is 300 W and laser scanning velocity of 960 mm/s. Therefore, these laser parameters were used for fabricating the SS316L and IN718 CGA.

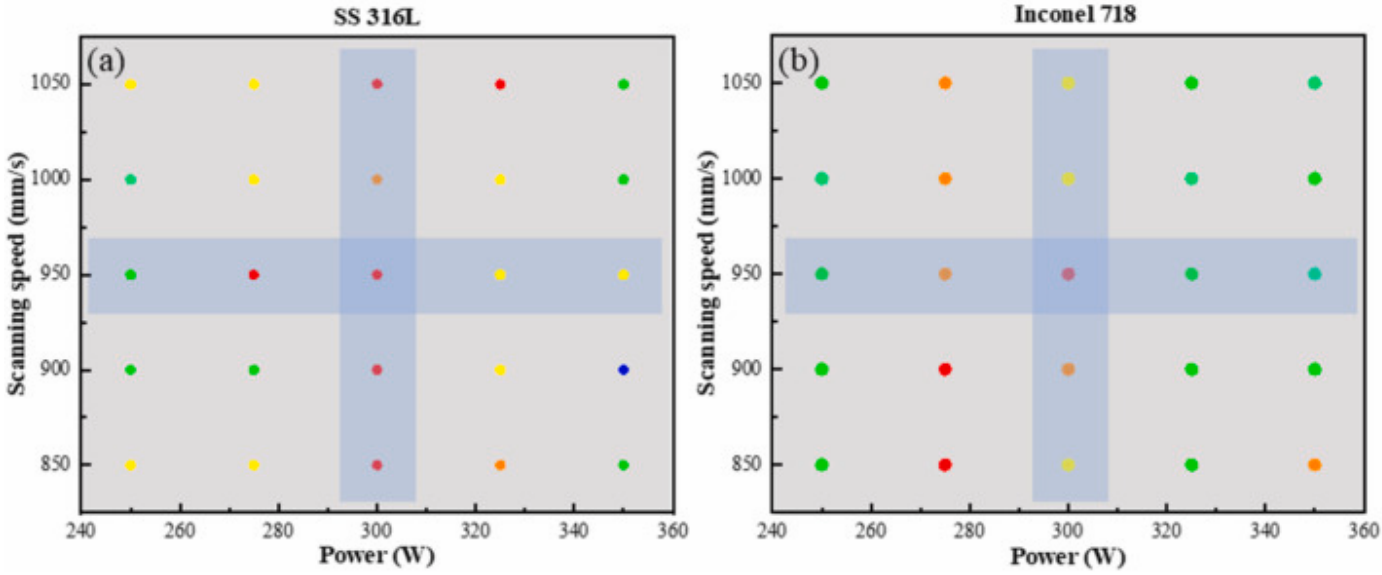

1. Download: Download high-res image (303KB)
2. Download: Download full-size image

Fig. 2. Process parameter maps for LPBF fabrication of (a) SS316L and (b) IN718. Color map provides a scale of relative densities. (For interpretation of the references to color in this figure legend, the reader is referred to the Web version of this article.)

3.2. Chemical composition of the SS316L/IN718 CGA

The composition variations of the seven main elements, Fe, Ni, Mo, Cr, and Nb in the SS316L/IN718 build along GD were investigated. Fig. 3 (a) shows the wt.% distribution of these constituents, measured by EDS. For comparison, the expected distributions of these constituents were also displayed in the same plot. Note that the experimentally obtained and expected values of compositions can be distinguished by the presence of standard deviation markers on the former. A close match between the experimental and expected distributions suggests that the methodology to fabricate the CGA and the process parameters employed were appropriate. Fig. 3 (b) shows the XRF composition maps of the 5 major constituents on the entire cross section parallel to GD and BD. The gradual change in color contrast of each element along GD further confirms that the composition gradient in the CGA is relatively smooth. The consistency of color at various positions along BD demonstrating the stability of powder laying. This is a significant improvement over prior work on the fabrication of SS304L/IN625 CGAs via DED, where large compositional fluctuations are observed along the GD [26]. From the elemental distribution, it was determined that for every 1 mm distance away from each end, along the GD, there is a 0.8 wt% change in the relative alloy concentrations of SS316L and IN718.

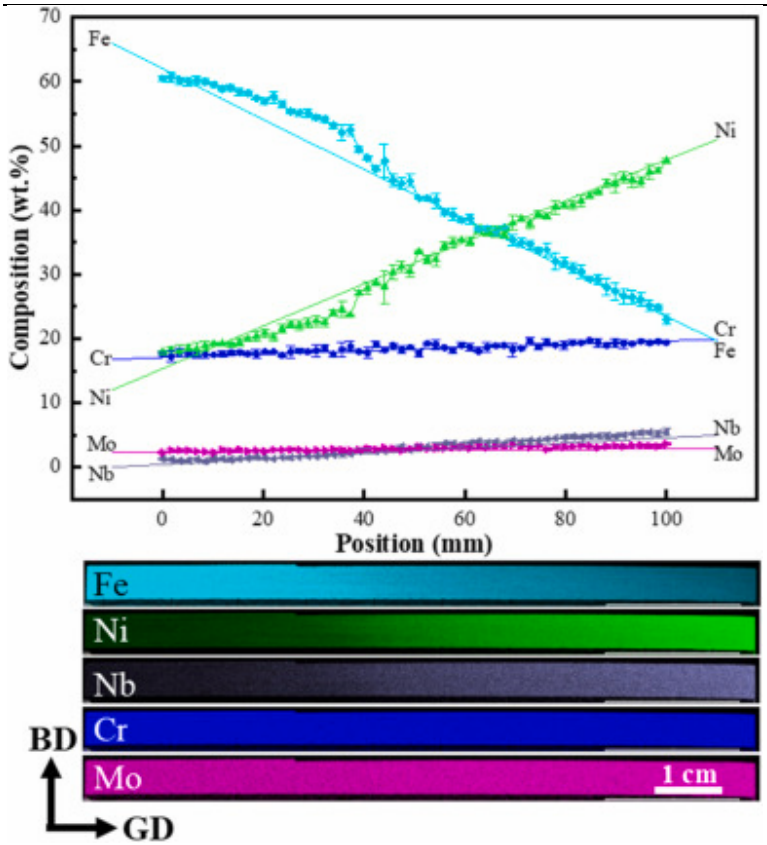

1. Download: Download high-res image (495KB)
2. Download: Download full-size image

Fig. 3. Chemical composition distribution along the gradient direction measured via (a) EDS and (b) the chemical composition map on the plane parallel to GD and BD of the CGA measured via XRF.

3.3. Microstructure and phase evolution of as-built and heat-treated SS316L/IN718

Cross-section slices with 10, 50 and 90 wt% of IN718 were extracted perpendicular to GD from the as-built SS316L/IN718 CGA and their representative microstructures are shown in Fig. 4 (a), (b) and (c), respectively. In all the slices, meso-structural features in the form of arc shaped boundaries, with a radius of 50–100 μm, are observed and marked with white dotted lines. These arc shaped features are characteristic of the melt-pools that form during LPBF. From the peripheries of these boundaries, columnar grains grow epitaxially along the build direction, which is indicated by the white arrow in Fig. 4 (b). The average grain sizes (measured as width of the columnar grains) in different cross sections are measured and listed in Table 2 (The grain size was measured via EBSD, which will be discussed subsequently in this section. All boundaries, whose misorientation >10° is considered a grain boundary while those with misorientation angle >2° but <10° is mapped as a sub-grain boundary.). Average grain sizes in slices are similar and fall in the narrow range of ~24–31 μm. The magnified images of these grains are shown in Fig. S1. Within these columnar grains, 0.6–0.8 μm sized sub-grains are also observed, which form due to interaction of convection currents (also referred to as the Marangoni effect) with the solidification front in the melt pool [27]. Note that the average size of the sub-grains is similar in all cross-section slices. Higher magnification imaging did not reveal the presence of secondary phases or precipitates in any of the slices, indicating that the overall microstructure of the CGA is quite homogeneous. The microstructural features in different slices along the GD contrasts with results obtained in prior studies. Kim et al. [14] developed a similar SS316L/IN718 CGA via DED and observed variations in grain morphology at different locations along the GD and observed the formation of Nb and Mo rich precipitates in the inter-dendritic regions. In another investigation of DED manufactured SS316L/IN718 CGA, Wu et al. [18] observed that the microstructure undergoes a columnar to equiaxed transition along the GD.

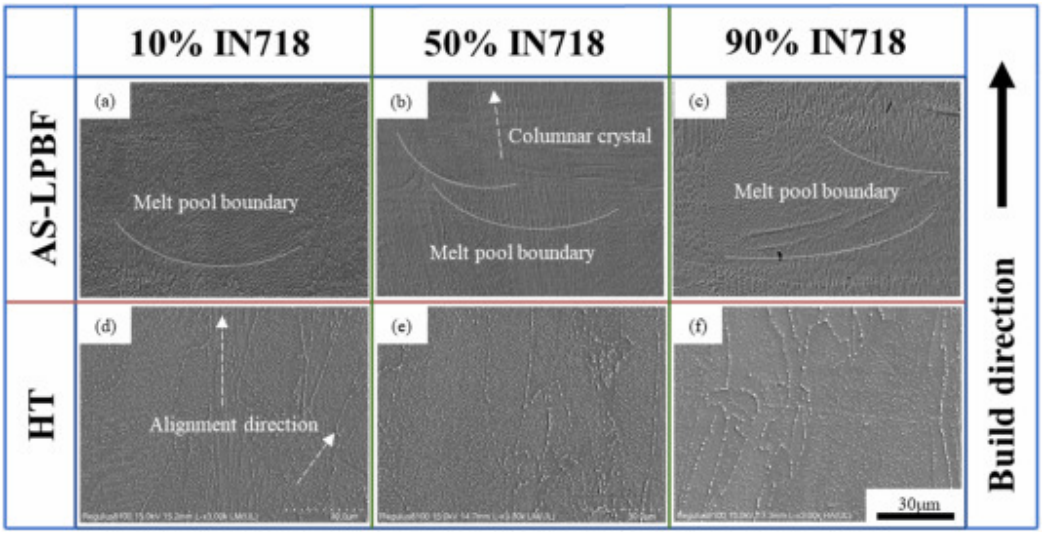

1. Download: Download high-res image (666KB)
2. Download: Download full-size image

Fig. 4. Representative microstructures of the CGA along GD in as-built condition for cross sections with (a) 10 wt%, (b) 50 wt% and (c) 90 wt% IN718; (d)–(f) Corresponding microstructures of these cross sections of the CGA in the heat-treated condition, respectively.

Table 2. The average grain size and Taylor factors of cross sections in SS316/IN718 CGA.

Empty Cell	Empty Cell	**10%IN718**	**50%IN718**	**90%IN718**
Grain size (μm)	As-Built	31.89 ± 17.02	24.48 ± 14.69	26.57 ± 16.61
	Heat treatment	25.36 ± 15.92	23.07 ± 12.71	21.05 ± 10.73
Taylor factor	As-Built	2.89	3.04	2.99
	Heat treatment	2.83	3.02	2.94

After performing the prescribed DA heat treatment, the microstructure of the cross-section slices, with 10, 50 and 90 wt % IN718, in SS316L/IN718 CGA are investigated. Their microstructures are shown in Fig. 4 (d), (e) and (f), respectively. Traces of the melt pool boundaries disappear in all the slices and the microstructure contains a mixture of columnar and equiaxed grains. The average grain sizes at cross sections with 10, 50 and 90 wt % IN718 are calculated and shown in Table 2.

Several ~1–2 μm and ~100–200 nm sized precipitates were observed at the grain boundaries and within grains, respectively. It must be mentioned that such precipitates were not detected in individually fabricated and heat-treated SS316L and IN718 [28,29]. In the slices with 10 wt% IN718, the precipitates within the columnar grains are preferentially aligned along BD (see Fig. 4 (d)). Alternately, the same are randomly distributed within the grains in the slice that has 90 wt% IN718 (see Fig. 4f).

To further understand the microstructure evolution of the as-built and heat-treated SS316L/IN718 CGA, EBSD measurements were performed on cross-section slices that contain 10, 50, 90% wt. % IN718. The Y0 inverse pole figure maps and corresponding {100} pole figures of these three cross sections from the as-built CGA are shown in Fig. 5 (a), (b) and (c), respectively. A strong <001> texture along the BD is observed in all the cross sections. Next, the multiple-of-uniform-density (MUD) value, which characterizes the relative strength of a particular orientation compared to other orientations, for <001> texture is calculated for each cross section. The values of MUD for the cross sections with 10, 50, and 70 wt% IN718 are 12.78, 10.98, and 9.62, respectively, which suggests that the <001> texture is dominant in the CGA. A marginal reduction in the MUD for the sections with 50 and 70 wt% IN718 compared to that with 10 wt% IN718 indicates that the former experiences slightly weaker epitaxial growth. Weaker epitaxial growth is expected to reduce the width of grains, which is consistent with the observed trend in grains sizes in these cross-section slices (see Table 2). This is because Fig. 5 (d), (e) and (f) show the Y0 inverse pole figure maps and pole figures of these three slices after heat treatment. The IPF maps indicate the presence of relatively randomly oriented and coarser grains in each slice, compared to that in the as-built condition. To further understand the changes in the microstructure after heat treatment, the kernel misorientation (KAM) maps of the three cross-sections in the as built and heat-treated conditions are shown in Fig. S2. The presence of green shaded regions in KAM maps of all slices of the as built CGA reveals the presence of dislocation structures within grains. Similar regions, albeit with lesser intensity, in the heat treated CGA suggests that these dislocation structures are somewhat retained even after heat treatment. MUD of cross sections with 10, 50, and 70 wt% IN718 are 6.21, 5.47 and 3.66 (see Fig. 5), which also indicates that the <001> texture has weakened but the <111> texture in the CGA has become stronger.

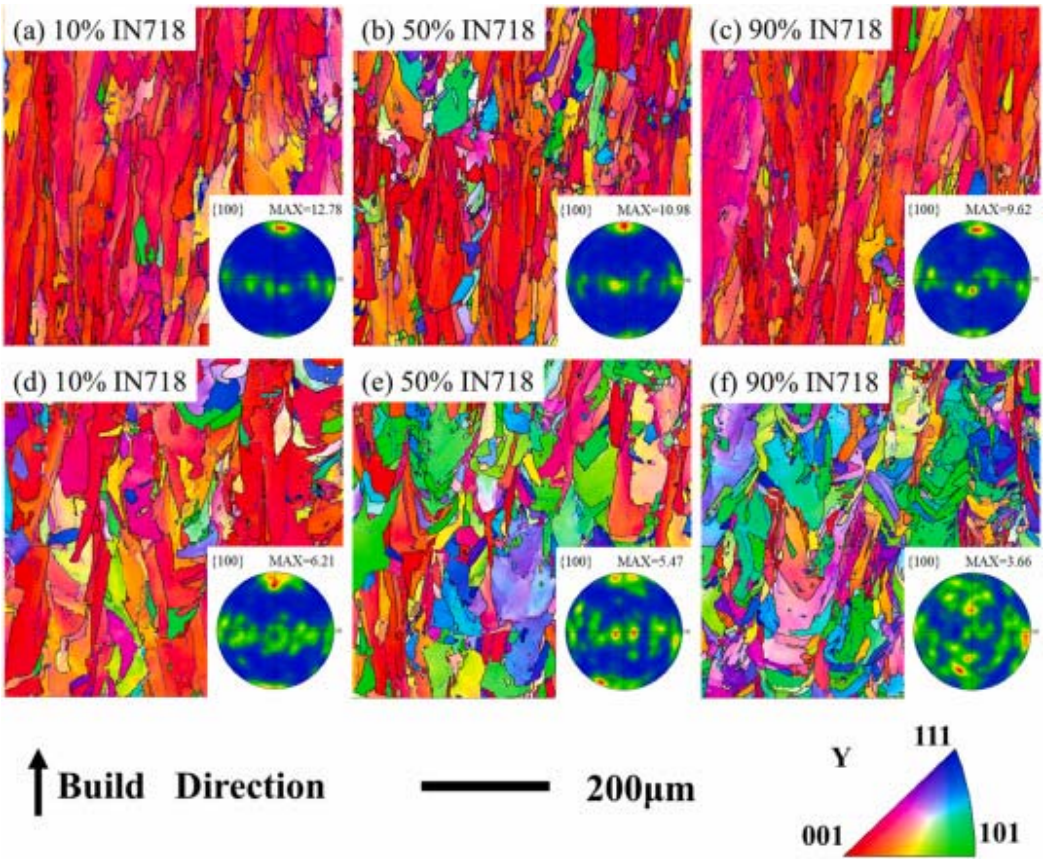

1. Download: Download high-res image (2MB)
2. Download: Download full-size image

Fig. 5. Inverse pole figures Y0 map and corresponding pole figures of as-built CGA with (a) 10 wt%, (b) 50 wt% and (c) 90 wt% IN718. (d)–(f) Corresponding maps of these cross sections in the heat-treated CGA, respectively.

From the EBSD data, the Taylor factor, *M*, for cross-section slices that contain 10, 50, 90% wt. % IN718 in the as-built and heat-treated CGA is extracted and listed in Table 2. In the cross sections with 10, 50, 90 wt% IN718, *M* is 2.89, 3.04 and 2.99, in the as-built condition, which reduces only slightly to 2.83, 3.02 and 2.94 in the heat-treated condition respectively. Note that the Taylor's factor has been calculated along X, which is the loading direction. A <100> fiber texture along Y direction (build direction) would result in random orientation in the X direction, that would explain the similar Taylor factor for different regions from the CGA sample.

Next, XRD was performed on as-built and heat-treated CGA to understand the different phases in them. The XRD scans on 10 cross-section slices taken at intervals of 10 wt % IN718 along the GD, are shown in Fig. 6 (a). In the as-built condition, peaks corresponding to the γ-FCC phase were detected in all cross sections of the CGA. The peak corresponding to (200) has the highest intensity compared to other peaks, which is attributed to the strong <001> texture of the CGA along the BD. XRD scans of the same cross-sections in the heat-treated CGA are shown in Fig. 6 (b). While peaks corresponding to the γ-FCC phase are still observed in all cross sections, the intensity of (111) peak is higher than that of (200). In addition, a few other peaks corresponding to

the Laves phase, which have a C14 crystal structure, were also identified in all the cross sections of the heat-treated CGA.

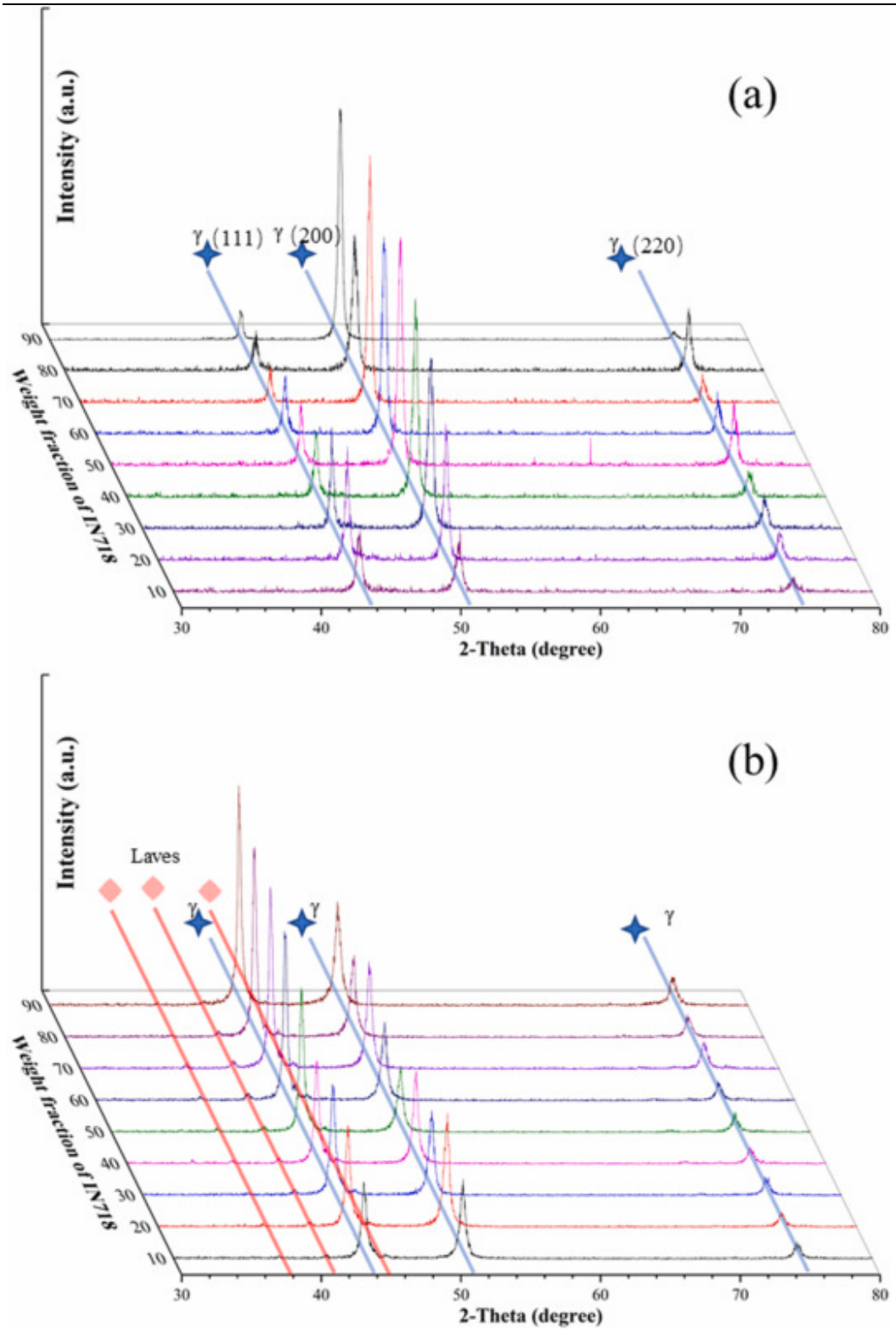

1. Download: Download high-res image (747KB)
2. Download: Download full-size image

Fig. 6. XRD scans of different cross sections along the GD of the (a) as-built and (b) heat-treated CGA.

To further characterize various microstructural phases, TEM was performed on the SS316L/IN718 CGA in the as-built and heat-treated condition. Fig. S3 (a), (b), (c) and (d) show the bright field TEM images of cross sections with 10, 25, 50, and 90 wt% IN718, respectively, in the as-built CGA. In all cross sections, the matrix consists of the γ phase along with some ~200 nm sized precipitates that have a dark contrast. These precipitates are periodically arranged in rows, and the average spacing between them is ~500 nm. The selected area electron diffraction (SAED) pattern of the dark precipitates in the cross section with 25 wt% IN718, shown in Fig. S3(b1), indicates that they are Laves phases. The volume fraction of the Laves phases, V_f^{Laves}, in the cross sections with 10, 25, 50, and 90 wt% IN718 are ~0.43%, ~2.03%, ~1.01% and ~1.45%, respectively. Considering that $V_f^{Laves} \leq 2\%$ in any cross section of the as-built CGA, it is not surprising that they were not detectable via XRD (see Fig. 6).

Fig. 7 (a), (b) and (c) display the bright field TEM images of cross sections with 10, 50, and 90 wt% IN718, respectively, in the heat-treated CGA along with their corresponding SAED images. In all images, grain boundaries are outlined by white dotted lines. The matrix of the cross section with 10 wt % IN718 (region enclosed within the yellow dashed box in Fig. 7 (a), consists of the γ phase, as indicated by the SAED patterns shown in Fig. 7 (a1). Several microns sized and nano scale Laves are observed at the grain interiors and grain boundaries, respectively. These precipitates are enclosed by green and brown dashed boxes and their corresponding SAED patterns are shown in Fig. 7 (a2) and (a3), respectively. Similar to what was seen in the images of the as built CGA, the Laves phases present within the grains are periodically arranged in rows, with an average spacing of ~500 nm. It is noteworthy that the spacing between the rows of the Laves phases matches well with the diameters of the dendritic columnar subgrains of the CGA in the as-built condition (see Fig. 4).

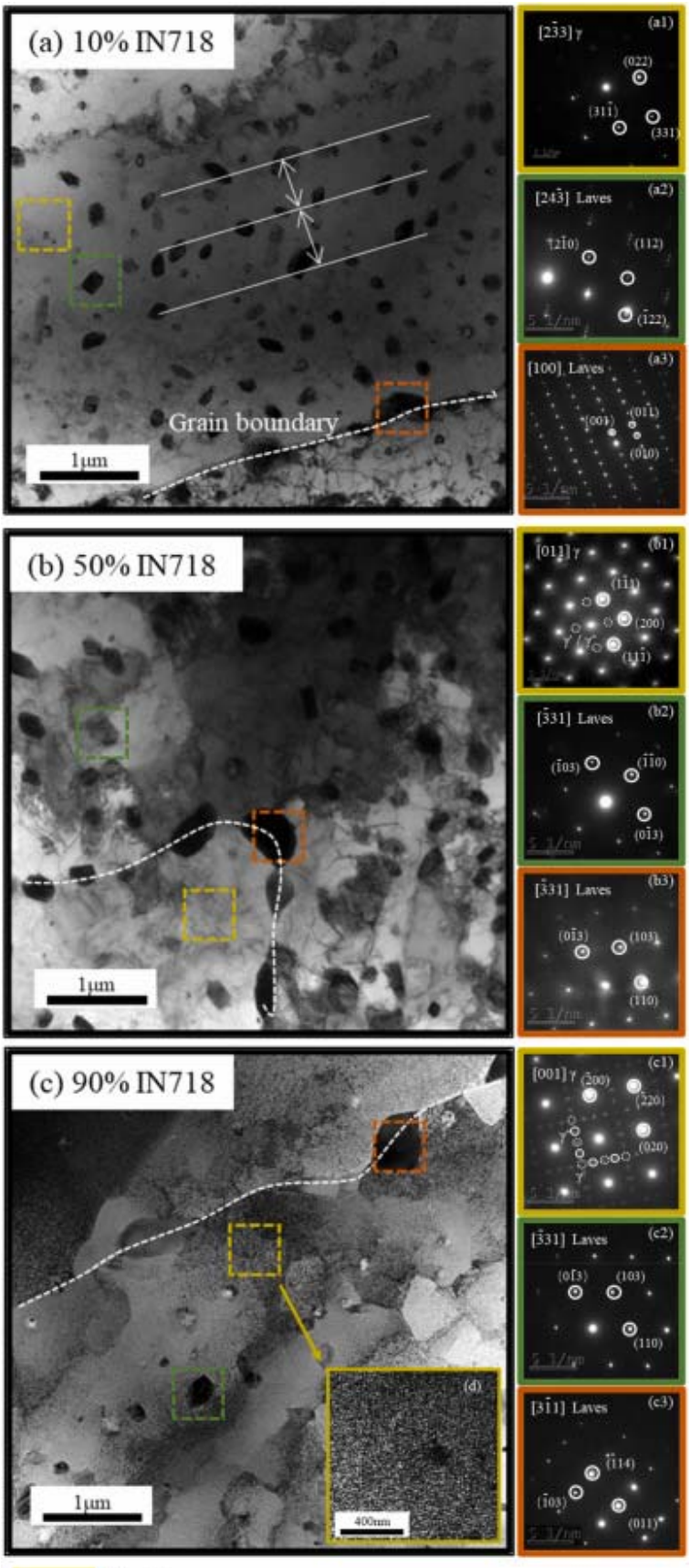
(a) 10% IN718
Grain boundary
1μm
(a1)
(a2)
(a3)
(b) 50% IN718
1μm
(b1)
(b2)
(b3)
(c) 90% IN718
1μm
(d)
400nm
(c1)
(c2)
(c3)
Matrix
Intragranular Precipitation
Grain Boundary Precipitation

1. Download: Download high-res image (1MB)
2. Download: Download full-size image

Fig. 7. Bright field TEM images of cross-sections with (a) 10 wt% (b) 50 wt% and (c) 90 wt% IN718 in the heat-treated CGA. Also shown are (a1)-(c1) SAED patterns of the matrix, (a2)-(c2) precipitates at the grain boundary, and (a3)-(c3) precipitates inside the grain, for these cross sections, respectively.

Using image analysis, it was determined that the volume fraction of Laves phases, V_f^{Laves}, is ~7.4%. The microstructural features in the cross section with 50 wt% IN718 (see Fig. 7 (b), (b1) and (b2)) are similar to those of the slice with 10 wt% IN718, with the sole difference that V_f^{Laves}, within the grains and at the grain boundaries, in it are ~5.2%. Alternately, the microstructure of the cross section with 90 wt % IN718 (see Fig. 7 (c), (c1) and (c2)) is distinctly different than that of the other two cross sections. Strong superlattice spots corresponding to the γ'' and the γ' precipitates, in addition to those of γ, were observed in its SAED pattern of the matrix. Inset of Fig. 7 (c) contains the higher magnification image of matrix regions where a fine, homogeneous distribution of γ'' and γ' is observed. Additionally, V_f^{Laves} in this cross section is ~3.3%, which is much lower than that in the cross section with 50 wt% IN718.

To further understand the precipitation of γ' and γ'' in the heat-treated CGA, cross sections with 60, 70, 80, 90 and 100 wt% IN718 are examined using high resolution SEM (HRSEM) imaging. Fig. 8 (a)-(d) show the HRSEM images of cross sections with 70, 80, 90, 100 wt % IN718, respectively. The cross section with 60 wt% IN718 does not have γ' and γ'' precipitates and is hence not shown here. The diameter of precipitates (or size) (r) is measured from these images and its distribution is shown in Fig. S4. A wide but unimodal distribution of r is observed in each cross section and the corresponding average diameters, r_{avg}, are measured and listed in Table 3. The table also lists the mean precipitate spacing, which is the distance between the centers of adjacent precipitates, (L). In the 4 cross sections considered, r_{avg} is broadly the same and ranges from 20 to 30 nm, although it marginally decreases with increasing wt.% of IN718. However, L decreases significantly with increasing wt.% of IN718 as it is 147.4 nm in the cross section with 70 wt% IN718 is but only 44.9 nm in that with 100 wt% IN718.

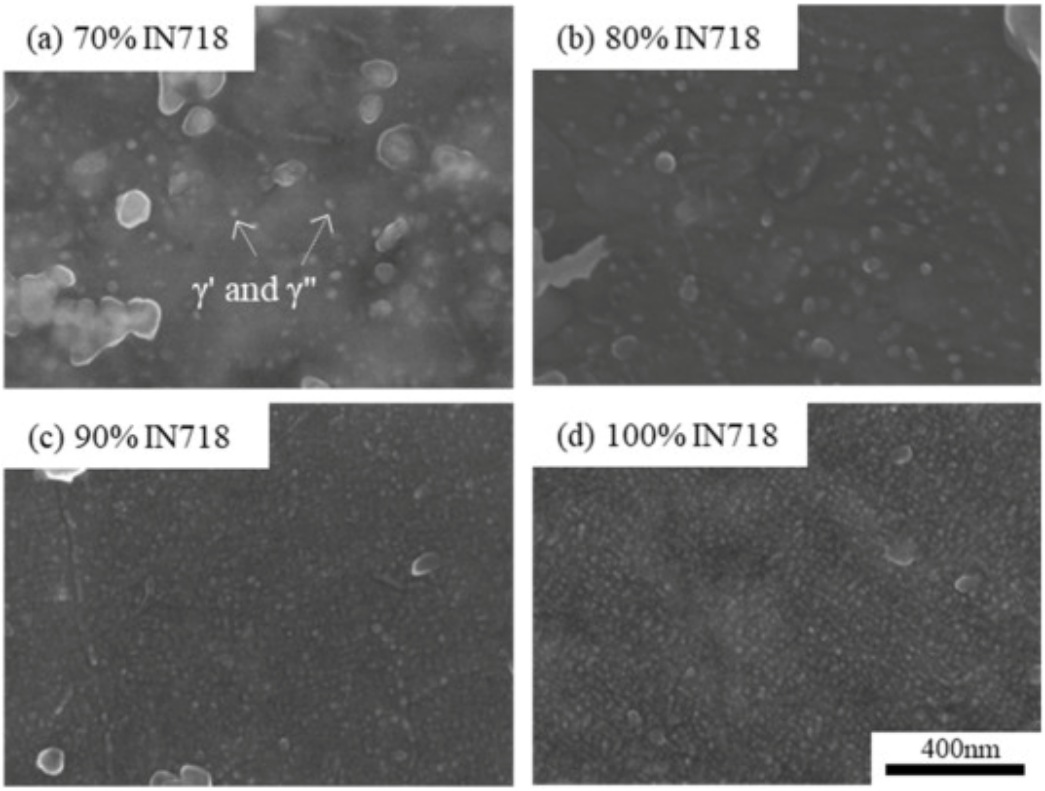

1. Download: Download high-res image (442KB)
2. Download: Download full-size image

Fig. 8. Representative HRSEM images of cross sections with (a) 70, (b) 80 (c) 90 and (d) 100 wt% IN718 in the heat-treated SS316L/IN718 CGA.

Table 3. The average size and the mean particle distance of the γ' and the γ''

Empty Cell	**70%IN718**	**80%IN718**	**90%IN718**	**100%IN718**
ravg **(μm)**	32.67	29.46	21.50	20.63
L **(μm)**	147.39	96.45	56.4	44.95

Next, the compositions of the Laves phases in the heat-treated CGA, measured by EDS, in cross sections with 10, 50 and 90 wt% IN718, are shown in Fig. 9. The Laves phases, irrespective of the cross section they are present in, contain Fe, Ni, Cr, Nb and Mo. This suggests that they are $(Fe, Ni, Cr)_2(Nb, Mo)$ Laves phases (Fe_2Nb type Laves phases). While the at. % of Cr, Nb and Mo in the Laves phases are the same in all cross sections, those of Fe and Ni vary with changes in the relative contents of SS316L and IN718 in CGA. As expected, cross sections with higher wt.% of SS316 have Fe-rich and Ni-poor Laves phases and the converse is true for cross sections with higher IN718.

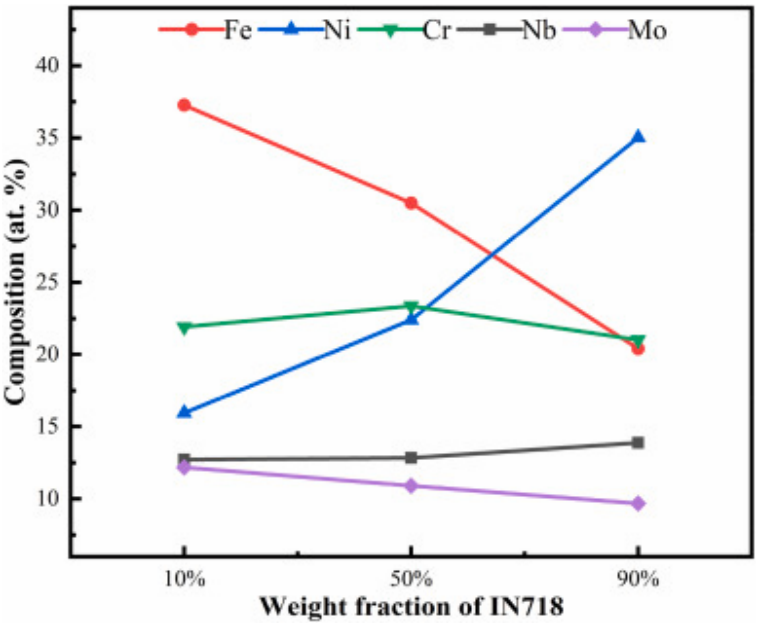

1. Download: Download high-res image (273KB)
2. Download: Download full-size image

Fig. 9. Chemical composition distribution of the Laves phases along the GD in the heat-treated CGA.

Overall, the microstructure of as-built SS316L/IN718 CGA is hierarchical as it contains 100–200 μm wide mesoscale solidified melt-pools, within which columnar grains with average width of 24 - 31 μm and 1 μm sized sub-grains are present at all locations along GD. The columnar grains are composed of the γ phase, which has an FCC structure and <001> dominant texture. Some 50–100 nm sized Laves phases at the grain interior and grain boundaries were observed in all cross sections. Regardless, along the GD, the microstructure, texture and sizes of different features are largely similar. After heat treatment, the microstructure in the CGA transforms to a mix of columnar and equiaxed grains, which have a weaker <100> texture. Moreover, there is limited grain growth as the average grain sizes are similar to that in the as-built condition. In sections of the heat-treated CGA containing ≥70 wt% of IN718, γ'' and γ' precipitates with average sizes of 20–30 nm form, whereas they are absent in sections with lower IN718 content. In addition, the Laves phases within the grains and at the grain boundaries in the as-built CGA, which are of the type $(Fe, Ni, Cr)_2(Nb, Mo)$, respectively, grow to larger sizes in all slices after heat treatment. Also, their total volume fraction first increases and then decreases with increasing in the IN718 content.

3.4. Simulated phase evolution in the SS316L/IN718 CGA

During LPBF, the melt pools in the build first solidify at a high cooling rate of ~10^3-10^7 K/s and thereafter experience multiple heating and cooling cycles as subsequent layers are deposited over them. However, in our simulations we have considered only the initial non-equilibrium solidification of the melt pool. It is also assumed that the constituents diffuse rapidly, assisted by the Marangoni convection, and get uniformly distributed in the melt pool. Using the Scheil formulation in Thermo-Calc along with the

Malac-Distmas platform, the proportions of γ and Laves phases in the CGA are calculated for different proportions of IN718 and SS316L. Fig. 10 shows the simulated fractions of these phases as a function of wt.% of IN718. In all cross sections, the fractions of FCC (γ phase) is ~ 100%. Laves phases, with phase fraction of 0.001%, first appear in the CGA cross section with 7 wt% IN718. Their phase fraction first increases to 0.1% and then to 1% when the IN718 content is increased to 10 and 25 wt%, respectively. For portions of the CGA that have 37–50 wt% of IN718, the fraction of Laves phases is ~0.9%, but with further increase in IN718 content, the fraction of Laves phases decreases, i.e. it is 0.01% when the IN718 content in the CGA is 90–100 wt%. Overall, simulations support the experimental observations that the as-built CGA predominantly consists of the γ phase and some Laves phases. Simulations also accurately predict that the phase fraction of the Laves phases becomes maximum when the IN718 content is 25 wt%.

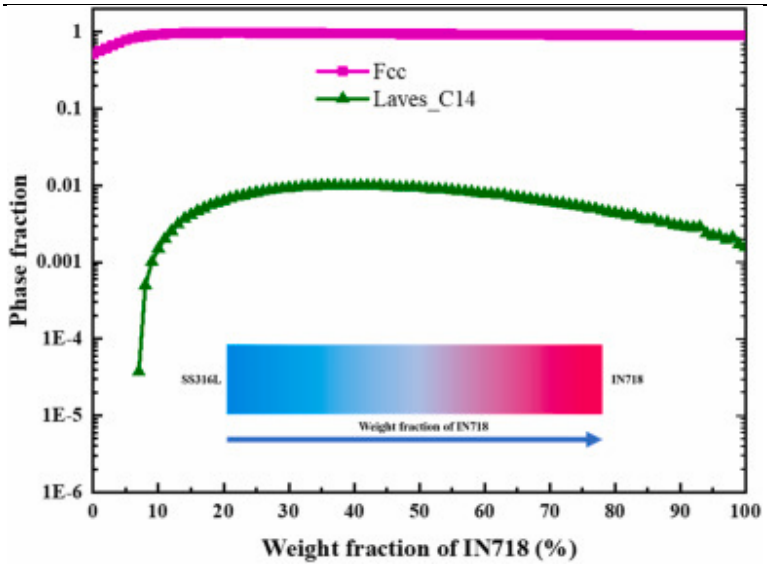

1. Download: Download high-res image (231KB)
2. Download: Download full-size image

Fig. 10. Calculated phase fractions of the matrix and Laves phases in the as-built SS316L/IN718 CGA along the GD based on Scheil-solidification.

3.5. Mechanical properties of as-built and heat-treated SS316L/IN718 CGA

The variations in the Vickers hardness, *H*, of the as-built and heat-treated CGA, measured from the SS316L rich side, along GD, is shown in Fig. 11. In general, *H* of the as-built and heat-treated CGA is low at the SS316L rich side but higher at the IN718 rich side. However, the increase in *H* in the heat-treated CGA is steeper than that in the as-built condition. In the as-built condition, at the location where the IN718 content is 0–45 wt%, *H* is ~250 ± 10 HV. With further increase in the wt.% of IN718, *H* monotonically increases and attains a maximum value of ~350 ± 20 HV at the location with 95 wt% IN718. Alternately, in the heat-treated condition, *H* is ~200 ± 25

HV in the portion with 0 wt% IN718. When the content of IN718 is ~45 and 100 wt%, *H* is ~250 ± 12 HV and 430 ± 10 HV, respectively. It is noteworthy that the variations in *H* are smoother for the as-built CGA than that in the heat-treated condition. Overall, the *H* of the CGA in both as-built and heat-treated conditions, increases along the GD with increasing content of IN718. The *H* of the CGA in the as-built condition is lower than that of the heat-treated condition in locations where the IN718 content is < 45 wt% and vice versa. This suggests that heat treatment strengthens and weakens the IN718 rich and SS316L rich portions, respectively, in the CGA.

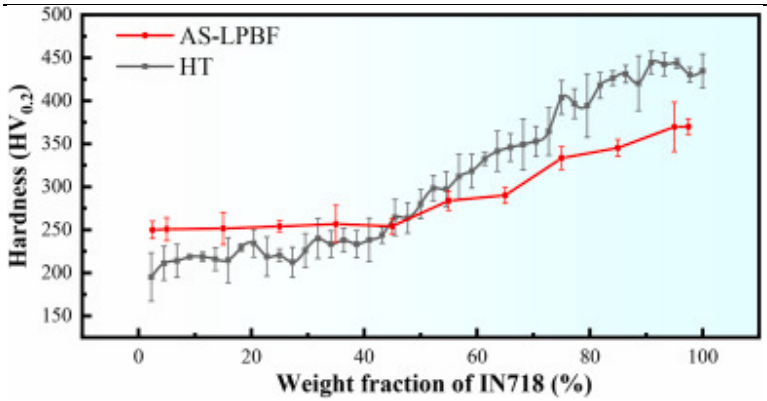

1. Download: Download high-res image (227KB)
2. Download: Download full-size image

Fig. 11. Hardness variations of the as-built and heat-treated SS316L/IN718 CGA along GD.

To further assess the mechanical properties of the CGA in the as-built and heat-treated conditions, uniaxial tensile tests were performed on its different cross section slices. Representative engineering stress (σ_E) versus engineering strain (ε_E) responses of the as built and heat-treated CGA on cross sections with 0, 8, 25, 48, 65, 82, 100 wt % IN718 are shown in Fig. 12 (a) and (b), respectively. The yield strength, σy, ultimate tensile strength (UTS) and elongation (ε_f) for each cross section is extracted and listed in Table 4. Cross sections with 0, 8 and 25 wt% IN718, have σy of ~ 547.7 ± 4.8, 522.7 ± 12.5 and 479.9 ± 6.5 MPa, respectively. This indicates that σy initially decreases (but only slightly) with increasing wt.% of IN718. With an increase in the content of IN718 to 48 wt%, σy significantly increases to 647 ± 28 MPa. Further increase in IN718 results in a gradual increase in σy, such that σy is ~ 809.5 ± 1.5 MPa in the cross section with 100 wt% IN718. A similar trend is observed in the variations of UTS with increasing IN718 content. For instance, UTS of slices with 0 and 25 wt% IN718 are 677 ± 5 and 537 ± 10 MPa, respectively. As the IN718 content is increased to 48 wt%, UTS increases to 777 ± 6 MPa. Finally, UTS attains a peak value of ~1047 ± 3 MPa in the cross section with 100 wt% IN718. While the trend in variations of ε_f with increasing IN718 content is also broadly similar to that of σy and UTS, there are some notable exceptions. For the cross section with 0 wt% IN718, ε_f ~ 32 ± 3.2%. However, ε_f drops precipitously to ~ 5 ± 1.1% in the slice with 25 wt% IN718. Although there is a gradual monotonic increase in ε_f with increasing wt.% of IN718, it only reaches a maximum value of ~ 15 ± 1.5% in the cross section with 82 wt% IN718. It is also worth noting from the σ_E- ε_E plots that beyond UTS, which corresponds to the point where necking initiates, there is negligible

elongation in many tensile samples. This means that the total uniform strain, ε_u is ~ ε_f in these specimens. Note that Considère's criterion for necking suggest that ε_u should be equal to the strain hardening exponent, n. n quantitatively characterizes the magnitude of strengthening in the material and its resistance to flow localization. For each specimen, n is obtained by fitting the portion of the flow curves between σ_y and UTS with the following power-law: $\sigma_T = K(\varepsilon_T)^n$, where K is a constant, σ_T is the true stress, and ε_T is the true strain. The values of n and the coefficient of determination for the fit, R^2, are listed in Table 4, Table 5 for the as-built and heat-treated CGA, respectively. For the cross section with 0 wt% IN718, n has a relatively high value of 0.216. However, there is a dramatic drop in n to 0.102 and 0.071 in cross sections with 8 and 25 wt% IN718, respectively. Further increase in IN718 content in the CGA gradually increases n from 0.124 to 0.173 in slices with 48 to 100 wt% IN718. It is also noteworthy that barring a few exceptions and within reasonable error, the magnitude and trend in variations of n matches well with that of ε_f. For instance, ε_f is half of that of n in the cross section with 25 wt% IN718.

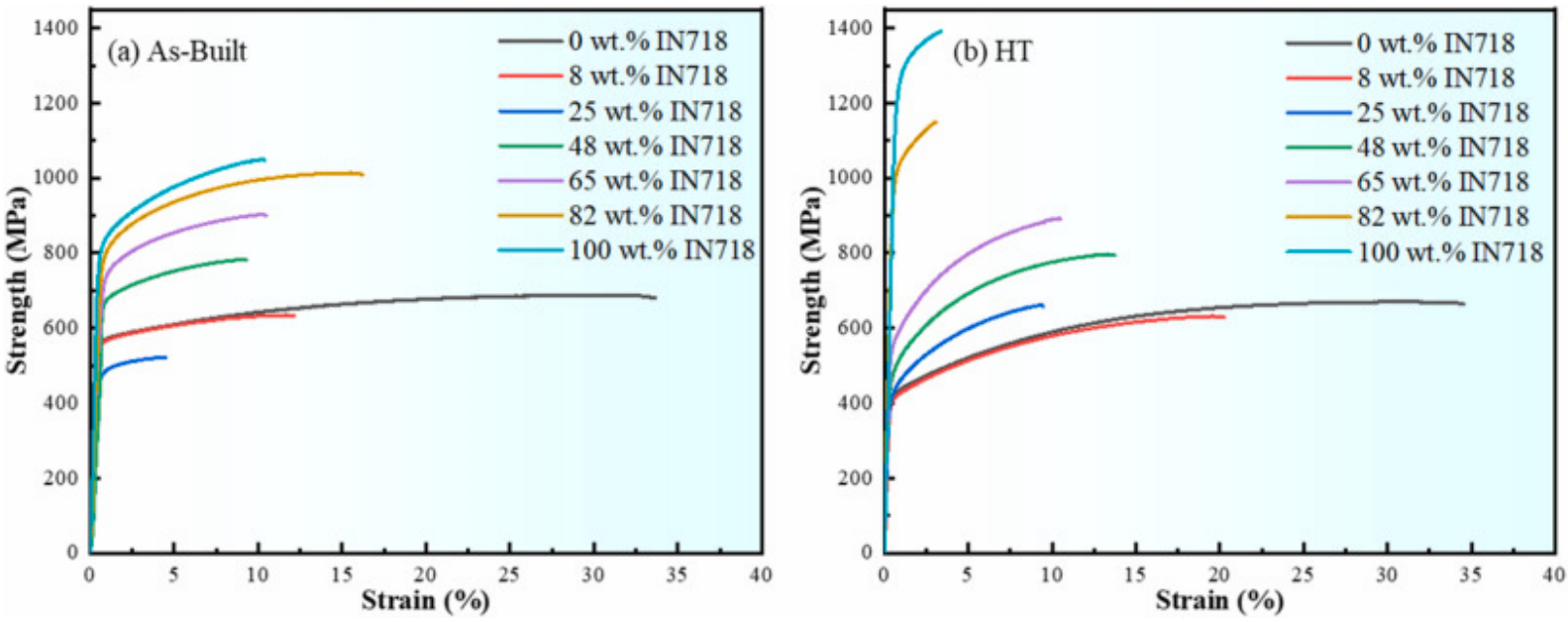

1. Download: Download high-res image (502KB)
2. Download: Download full-size image

Fig. 12. Representative engineering stress (σ_E) versus engineering strain (εE) curves of (a) as-built and (b) heat-treated CGA.

Table 4. Tensile properties, σ_y (yield strength), UTS (ultra-tensile strength), ε_f (elongation to failure), and n (strain hardening exponent), of different cross sections in the as-built CGA.

wt. % IN718	σ_y	UTS	ε_f	n	R^2
0	548 ± 5	677 ± 6	32 ± 3	0.216	0.996

wt. % IN718	σy	UTS	ε_f	*n*	R^2
8	523 ± 12	600 ± 19	12 ± 2	0.102	0.987
25	480 ± 7	537 ± 1	5 ± 1	0.071	0.999
48	647 ± 28	777 ± 6	10 ± 1	0.124	0.997
65	742 ± 13	901 ± 2	11 ± 2	0.134	0.998
82	769 ± 8	1002 ± 19	14 ± 2	0.163	0.998
100	810 ± 2	1048 ± 4	11 ± 2	0.173	0.998

Table 5. Tensile properties of different cross sections in the heat-treated CGA.

wt. % IN718	σy	UTS	ε_f	*n*	R^2
0	406 ± 4	647 ± 19	28 ± 6	0.288	0.999
8	403 ± 3	619 ± 9	20 ± 1	0.255	0.998
25	399 ± 11	621 ± 29	10 ± 2	0.235	0.998
48	472 ± 12	795 ± 17	13 ± 3	0.238	0.999
65	528 ± 17	861 ± 22	11 ± 1	0.232	0.999
82	965 ± 50	1115 ± 52	3 ± 0.2	0.193	0.997
100	1184 ± 9	1335 ± 36	3 ± 1	0.192	0.998

The values of σ_y, UTS, ε_f and *n* of different slices in the heat-treated CGA are listed in Table 5. Cross sections with 0, 8 and 25 wt% IN718 have the same σ_y of 400 MPa, within a reasonable margin of error. With further increase in IN718 content, i.e. in cross sections with 48 and 65 wt% IN718, σ_y increases marginally to 471 ± 12 and 527 ± 17 MPa, respectively. However, σ_y considerably increases to ~965 ± 50 and ~1184 ± 8 MPa, when the IN718 content is 82 and 100 wt%, respectively. Note that for cross sections of the CGA which have IN718 ≤ 65 wt%, the σ_y is lower in the heat-treated condition than that in the as-built condition. The converse is true when IN718 > 65 wt%, which suggests that heat treatment has a significant strengthening effect only above this composition of the CGA. The trend of variations in UTS, with increasing IN718 content, is identical to that of σ_y. The UTS is in the range of ~620–650 MPa for the cross sections with 0, 8 and 25 wt% IN718, but in those with 48 and 65 wt% IN718, UTS is 795 ± 17 and 861 ± 22 MPa, respectively. Finally, a dramatic increase of UTS to 1115 ± 52 and 1335 ± 36 MPa is observed in cross sections with 82 and 100 wt% IN718. Interestingly, the UTS of all the equivalent cross sections in as-built and heat-treated CGA are similar, except that which has 100 wt% IN718. The trend of variations of ε_f in the heat-treated CGA with increasing IN718 content is initially similar to that of the as-built CGA, i.e. it precipitously decreases from 28 ± 6% in the cross section with 0 wt% IN718 to ~10 ± 2% in the cross section with 25 wt% IN718. However, while ε_f marginally recovers to ~13 ± 3% with increase in the IN718 content to ~48 wt%, it again reduces to ~3% in cross sections with 82 and 100 wt% IN718.

Compared to the as-built CGA, *n* of the heat-treated specimens is significantly higher in all cross sections. In the cross sections with 0–65 wt% IN718, *n* ranges from 0.29 to 0.23. However, it drops slightly to 0.19 in cross sections with 82 and 100 wt% IN718. Additionally, while *n* is ~ ε_f in cross sections with 0 wt% IN718 and only 20% higher than ε_f in cross-sections with 8 wt% IN718, it is at least twice as high as ε_f in slices where IN718 content is ≥ 25 wt%. This suggests that cross sections in the heat-treated CGA that have IN718 content higher than 25 wt% undergo premature failure.

The fracture surfaces of the tensile-tested specimens, extracted from different cross sections of the as-built CGA with 8, 48 and 82 wt% IN718 are displayed in Fig. S5. All of them show rough and dimple features, which are characteristic of ductile failure. However, in the fracture surfaces of tensile tested specimens, extracted from the cross section with 25 wt% IN718, shown in Fig. 13 (a) and (b), several faceted features were observed. They suggest that the tensile sample underwent brittle intergranular fracture. A higher magnification images in Fig. 13 (c) reveal the presence of ~100 nm sized nano scale precipitates embedded over the faceted features. EDS analysis of these precipitates reveal that they are rich in Nb and Mo, suggesting that they are Laves phases. Incidentally, σ_y, UTS and ε_f of the cross section with 25 wt% IN718 are the lowest compared to that of others in the as-built CGA.

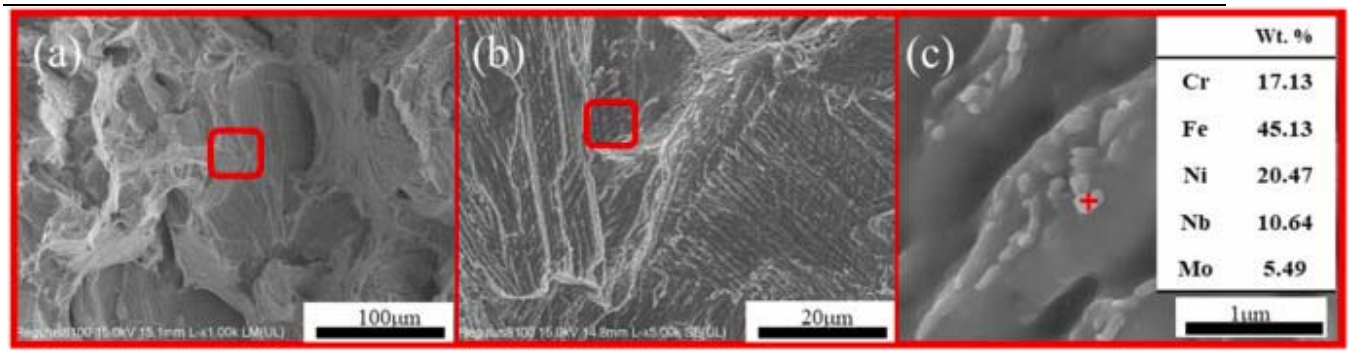

1. Download: Download high-res image (476KB)
2. Download: Download full-size image

Fig. 13. Fracture surfaces of the tensile-tested cross section with 25 wt % IN718 in the as-built CGA.

The fracture morphology of tensile tested specimens, extracted from cross sections of the heat-treated CGA with 8, 48 and 82 wt% IN718, are shown in Fig. S6. Fracture surfaces of all cross sections exhibit a rough and dimpled morphology, which suggests that all of them underwent ductile fracture.

Overall, the variations of σ_y and UTS in the as-built and heat-treated CGA is similar to that of H, i.e., they also increase with increasing IN718 content. However, after the heat treatment, σ_y and UTS of the build is much lower than that of the as-built condition for cross sections with <65 wt%IN718. Alternately, the UTS and σ_y of the heat-treated CGA increases significantly, compared to that in the as-built condition, in portions where the IN718 content is ≥ 82 wt%. The cross section with 25 wt% IN718 in the as-built CGA, has a significantly lower σ_y and UTS compared to all other cross sections. Fractographic investigations reveal that this cross section undergoes intergranular fracture, whereas

others, in the as-built and heat-treated build, exhibit ductile fracture features. Finally, ε_f of the as-built and heat-treated CGA is highest for the cross section with 100 wt% SS316L but drops sharply when the IN718 content is increased. While further increase in IN718 content marginally improves ε_f, it remains lower than half of that in the cross section with 100 wt% SS316L. A cross section-wise comparison of ε_f of the CGA in the as-built and heat-treated condition reveals that ε_f is mostly unaffected by heat treatment. The main exception are cross sections with >8 wt% IN718 in the heat-treated CGA, where the ε_f is one-third of that in the as-built CGA. Finally, the trend in variations of n with increasing IN718 content in the as-built and heat-treated CGA match well with that of ε_f. While $n \sim \varepsilon_f$ or 20% higher or lower than ε_f in most cross sections of the as-built CGA (barring 0 wt% IN718), the same is not observed for the heat-treated CGA.

4. Discussions

4.1. Microstructure and phase evolution in the as-built and heat-treated CGAs

The optimization of processing parameters for LPBF of SS316L/IN718 CGA needs to ensure synchronous melting of the two constituent powders besides maximizing its density. The absence of unmelted particles of IN718 or SS316L in the microstructure indicates that the two alloys mix intimately in the molten state. Note that this molten mixture forms within mesoscale sized 'melt pools' from which heat is extracted by the surrounding unmelted alloy powder mixture and substrate. As a result, the molten mixture undergoes directional solidification, which initiates at the melt pool boundaries. Directional solidification is accompanied by formation of columnar grains whose axes are parallel to BD, as seen in different cross sections of the CGA build (see Fig. 4, Fig. 5 (a)–(c)). The absence of a thermal gradient along GD ensures that the grain size in the build, at different cross sections, do not vary significantly. Within these grains are cells, which as previously noted, are the outcome of the non-equilibrium cooling of the melt. Similar cellular structures were observed in several other LPBF fabricated steels and superalloys and a careful examination of them revealed that the cell boundaries are finely distributed dislocations [30]. One of the possible mechanisms for the formation of dislocation cells during LPBF of these alloys is as follows [31]. During solidification, dislocations are formed to accommodate thermal strains in the melt-pools during solidification. Since these melt-pools are subjected to additional heating and cooling cycles during processing, these dislocations attain a cellular configuration to facilitate energy minimization [31].

Throughout the build, the FCC γ phase forms as it's the most stable phase for both alloys. These γ grains have the <001> texture (see Fig. 5) as this is the preferred growth orientation of the directionally solidified FCC phase. In addition, the mixing of IN718 and SS316L produces Laves phases (see Fig. 10), which was also reported in prior studies on IN718 containing CGA alloys [32]. During solidification of the melt, a solute lean γ solidifies first, which leads to the segregation of Nb and Mo to the melt. At the final stage of solidification, these segregated constituents react and form Laves phases at the grain boundaries. Since IN718 contains significant amount of Nb and Mo, the formation of Laves phases is increasingly favored when its proportion increases in the alloy mixture [16,33]. This aspect is confirmed in both experiments and simulations as the V_f^{Laves} in cross section with 25 wt% IN718 is higher than that in the cross section with 8 wt% IN718 (see Fig. 10 and S4(c)). However, it was also observed that V_f^{Laves} is the highest in the cross section with 25 wt% as it again decreases when the wt.% of IN718 is increased further (see Fig. S3). The decrease in V_f^{Laves} with increasing IN718 in the CGA is also confirmed by thermodynamic simulations (see Fig. 10), which indicates that Fe-rich Laves phases, which form in the SS316L rich portion, have a lower enthalpy of formation than Ni-rich Laves phases that form in the IN718-rich end.

After heat treatment, the SS316L/IN718 CGA undergoes the following microstructural changes. During the subsequent two-step ageing, γ" and γ' precipitate from the supersaturated γ phase. Owing to the higher Nb content than Al in IN718, γ" (Ni_3Nb) is

the more abundant primary precipitate, compared to γ' (Ni_3Al), that forms during ageing [[34], [35], [36]]. However, TEM results suggest that significant volume fractions of both γ" and γ' form only when the IN718 content >70 wt% (see Fig. 8). Alternately, in the portions of the CGA with <70 wt% IN718, the Laves phases at the grain boundaries coarsen and several new Laves precipitates form inside the grains. Laves phases also form within grains of the heat-treated CGA, and have a characteristic spacing between them. The formation of Laves phases with a characteristic spacing is attributed to the following two overlapping length scales in the as-built microstructure, the inter-dendritic spacing and cell size. Since the melt pools undergo dendritic solidification, solutes that are released from the dendrites, segregate at the inter dendritic spaces. During annealing, these segregated solutes combine and form the Laves phases. The boundaries of cells, which consist of several dislocations, also promote the precipitation of Laves phases by facilitating rapid diffusion of Nb and Mo along them (see Fig. 7) [37]. This is because dislocation networks lead to lattice distortion, which elevates the diffusion rate of solutes. Furthermore, the precipitation of these phases at the cell boundaries will also relieve the strain energy associated with the dislocation networks.

Note that the cross section with 10 wt % IN718 has a more dominant <100> texture than those with higher IN718 content, which implies that it retains a higher proportion of the as-built cell structure with dislocation networks after heat treatment. The cell size in the as built CGA is ~0.8 μm, which is also approximately equal to the spacing between the Laves phases in the heat treated cross section with 10 wt% IN718. Given that these dislocation networks facilitate fast diffusion, the Laves phases in the former are more closely spaced than those in the latter.

4.2. Deformation behavior in as-built and heat-treated SS316L/IN718 CGAs

In both as-built and heat-treated SS316L/IN718 CGA, the microstructural variations at different cross sections along the GD holds the key to understanding differences in their mechanical properties. In the following sections, the parameters contributing to strengthening and deformation characteristics of different portions of the CGA are discussed in detail.

4.2.1. Strengthening mechanisms in the as-build SS316L/IN718 CGA

For any alloy, σ_y can be expressed a summation of the intrinsic lattice friction stress σ0, grain boundary strengthening, $\Delta\sigma_{HP}$, dislocation strengthening, $\Delta\sigma_{DS}$, solid solution strengthening, $\Delta\sigma_{SS}$, and precipitation hardening, $\Delta\sigma_{PS}$, which is,

$$\sigma_y = \sigma_0 + \Delta\sigma_{HP} + \Delta\sigma_{DS} + \Delta\sigma_{SS} + \Delta\sigma_{PS} \quad (1)$$

Given that both γ" and γ' precipitates are not present and that $V_f^{Laves} \leq 2\%$ in the as-built CGA, the contribution of $\Delta\sigma_{PS}$ to strengthening will be negligible. Other contributions to σ_y are calculated from the following method. The intrinsic lattice friction stress σ_o is a material constant and is expressed as [38],

$$\sigma_0 = M \bullet \tau_{crss} \quad (2)$$

Where τ_{crss} is the critical resolved shear stress. As mentioned earlier, *M* is in the range of ~2.89–3.04 in different cross sections of the as-built CGA (see Table 2). For pure Ni and γ-Fe, τ_{crss} = 17.5 and 16 MPa, respectively [[38], [39], [40]]. For simplicity, the weighted average of the τ_{crss} was calculated by considering the proportions of Fe and Ni at each location in the CGA along the GD and then used for calculating σo in eq. (2).

$\Delta\sigma_{HP}$ is calculated from the Hall-Petch relationship [41],

$$\Delta\sigma_{HP} = k_{HP} \bullet d^{-\frac{1}{2}} \quad (3)$$

where k_{HP} is the Hall-Petch coefficient and d is the grain size. For IN718, and SS316L, k_{HP} is 710 and 253.6 MPa $\mu m^{1/2}$, respectively [42,43]. For each cross section, the weighted average of k_{HP} is calculated, as was previously done for τcrss in eq. (2). Thereafter, using d obtained from Table 2, $\Delta\sigma_{HP}$ was calculated for each cross section using eq. (3). Note that several studies have considered *d* as the cell size to calculate the contribution of strength from grain boundaries [[44], [45], [46]]. However, this study considers the grain size as *d* for calculations of $\Delta\sigma_{HP}$ as this helps in matching the analytical and experimentally obtained values of total strength. Next, $\Delta\sigma_{DS}$ is calculated from the Bailey-Hirsch relation, which is [47],

$$\Delta\sigma_{DS} = M\alpha Gb\rho^{\frac{1}{2}} \quad (4)$$

where α = 0.2 is a constant for FCC crystals, G ~80 GPa, is the shear modulus, b ~0.25 nm is the Burgers vector of the crystal and ρ is the dislocation density (*G* and *b* of both alloys is similar). For calculations, the geometrically necessary dislocation (GND) density, obtained from EBSD results in different cross sections and listed in Table 6, are considered as ρ. Note that this is not strictly correct as ρ in eq. (4) corresponds to dislocation density of statistically stored dislocations (SSD), which are primarily responsible for slip and accommodate plastic deformation. Generally, SSDs constitute ~70% of the total dislocation density of the crystal. However, since we were unable to get an estimate of SSD density, we have assumed that their density is approximately equal to that of GND density.

Table 6. The GND of different cross sections in the CGA.

Empty Cell	**10%IN718**	**50%IN718**	**90%IN718**
As-built (10^{14} m^{-2})	4.6416	4.1868	3.8928
Heat-treated (10^{14} m^{-2})	0.10975	0.08254	0.08771

For estimating the contribution from $\Delta\sigma_{SS}$ at each cross section, the weighted proportions of Ni (Inconel 718) and Fe (SS316L) were considered as the solvent matrix [39,[48], [49], [50], [51], [52], [53]]. ΔσSS, is estimated using the method of Gypen and Deruyttere [54,55]:

$$\Delta\sigma_{SS} = \left(\sum \beta_i^{3/2} c_i\right)^{2/3} \quad (5)$$

where βi represents the solution strengthening coefficients of solute element i in the binary nickel alloys and are listed in Table 7 [56], ci is the solute concentration of elements i in the Ni matrix. Owing to the rapid solidification during LPBF, precipitation is inhibited and most of the solute atoms are dissolved in the solvent matrix.

Table 7. Parameters for strengthening mechanism calculation.

Parameter	Value	Parameter	Value
M	~3	βAl	225 MPa at %$^{-1/2}$
kHP	(253.6/710) MPa·μm$^{1/2}$	βTi	775 MPa at %$^{-1/2}$
α	0.2	βCr	337 MPa at %$^{-1/2}$
G	80 GPa	βMn	448 MPa at %$^{-1/2}$
b	0.25 nm	βFe	153 MPa at %$^{-1/2}$
γ''_{APB}	296 mJ/m^2	βNb	1183 MPa at %$^{-1/2}$
υ	0.29	βMo	1015 MPa at %$^{-1/2}$

Using eqs. (1), (2), (4), (5), the calculated σ_y is plotted in Fig. 14. Contributions from each strengthening mechanism is represented by shaded polygonal areas and the experimentally measured σ_y is also included for comparison. The calculated σ_y for all cross sections matches well with the experimentally measured values, except that of the cross section with 25 wt% IN718. The disparity between the experimentally measured and calculated σ_y in the cross section with 25 wt% IN718 is due to the highest VfLaves in it (see Fig. 10 and Fig. S3). Note that the formation of Laves phases, which do not contribute to precipitation strengthening, except at higher temperatures, consumes some of the dissolved constituents in the matrix. Therefore, $\Delta\sigma_{SS}$ determined from eq. (5), which assumes that all the constituents are in solid solution, overestimates the contribution of solid solution strengthening in this cross section.

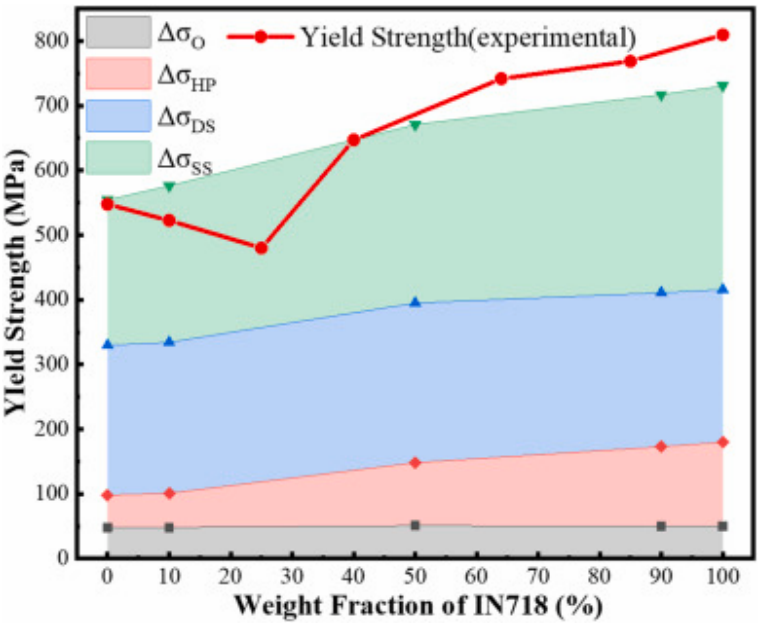

1. Download: Download high-res image (284KB)
2. Download: Download full-size image

Fig. 14. Contributions of different strengthening mechanisms to σ_y in the as-built CGA along GD. The experimentally obtained values of σ_y are included for reference.

4.2.2. Strengthening mechanisms in the heat-treated SS316L/IN718 CGA

On performing the DA heat treatment on the CGA and the sub-grains disappear (see Fig. 4, Fig. 5). Therefore, while the GND is relatively lower in the heat-treated CGA compared to that in its as-built condition, their overall grain sizes are similar (see Table 2, Table 6). Moreover, although the <100> texture weakens in the heat-treated CGA, compared to that in the as-built condition, a significant change in *M* is not observed (see Table 2). Also, γ'' and γ' precipitates are not present in cross sections of the CGA that have <70 wt% IN718, which implies that the contribution of $\Delta\sigma_{PS}$ to σ_y can be neglected. Therefore, the strengthening contributions to σ_y in the cross sections of the heat-treated CGA with IN718 < 70 wt% will be slightly lower than that of the as build condition (see section 4.2.1), owing to the relatively lower contribution of ΔσDS. This is consistent with the observation that the heat-treated CGA, in all cross sections with <70 wt% IN718, has lower experimentally measured σ_y compared to their counterparts in the as-built condition (see Table 4, Table 5). In addition, the reduction in σ_y is also attributed to the coarsening and additional precipitation of Laves phases within these cross sections of the heat-treated CGA (see Fig. 7), which further depletes the matrix of solutes. As observed earlier in the as-built CGA cross section with 25 wt% IN718, this depletes solutes in the matrix and reduces the actual contribution of solid solution strengthening to the measured σ_y.

Similarly, in cross sections of the heat-treated CGA with ≥70 wt% IN718, there will be a reduced contribution of $\Delta\sigma_{DS}$ to σ_y compared to that in its as-built condition. Moreover, these cross sections also contain γ' and γ'' phases (See Fig. 8), in addition to Laves

phases, which will further reduce the solute concentration in the matrix compared to that in the rest of the CGA. Therefore, the contribution of $\Delta\sigma_{SS}$ to σ_y will be least in the portions of the CGA with ≥70 wt% IN718. However, there in an increased contribution of $\Delta\sigma_{PS}$ to σ_y in these cross sections of the CGA. In fact, the 80% increase in the experimentally measured σ_y of cross sections with ≥70 wt% IN718 in the heat-treated CGA compared to that in the as build condition suggests that the contribution of $\Delta\sigma_{PS}$ more than compensates for reduced contribution of $\Delta\sigma_{SS}$ and $\Delta\sigma_{DS}$ (see Table 4, Table 5). Strengthening from precipitates can originate from their shearing by dislocations, $\Delta\sigma_{sh}$, or when dislocations bypass them via the Orowan bypass mechanism, $\Delta\sigma_{Oro}$ [53]. The operating mechanism is governed by the energy minimization principle and also depends on the size and coherence of the precipitates. Galindo-Nava revised the weak and strong pair-coupling precipitate shearing mechanism, and suggested that $\Delta\sigma_{sh}$ is expressed in terms of r, the effective length of the dislocations driving particle cutting (Λ), precipitate volume fraction (f), the anti-phase boundary energy of the precipitate (γ_{APB}), the segment length of cutting a precipitate (l) and mean particle spacing (L) [53], which is as follows,

$$\Delta\sigma_{sh} = \frac{M\gamma_{APB}l}{2b(\Lambda+2r)} \tag{6}$$

Where l, Λ, L are determined from,

$$l = \begin{cases} 2r if\ r < \frac{Gb^2}{2\gamma_{APB}} \\ 2\left(r^2 - \left(r - \frac{Gb^2}{2\gamma_{APB}}\right)^2\right)^{1/2} if\ r \geq \frac{Gb^2}{2\gamma_{APB}} \end{cases} \tag{7}$$

$$\Lambda = \max\left\{L\left(Gb^2/2r\gamma_{APB}\right)^{1/2}, L - l\right\} \tag{8}$$

The Orowan bypass mechanism for precipitation strengthening is as follows [57],

$$\Delta\sigma_{Oro} = M\frac{0.4Gb}{\pi\sqrt{(1-\upsilon)}}\frac{\ln(2r/b)}{L} \tag{9}$$

where υ is the Poisson's ratio of the alloy. On comparing eq. (6), (9), it is evident that $\Delta\sigma_{Oro}$ is independent of the precipitate characteristics, whereas γ_{APB}, has a significant influence on $\Delta\sigma_{sh}$. Precipitates with higher γ_{APB} provide greater resistance to shear by dislocations, which leads to increased $\Delta\sigma_{sh}$. In IN718, γ_{APB} of γ'' is ~296 mJ/m^2 whereas that of γ' is only 12 mJ/m^2 [58]. This suggests that $\Delta\sigma_{sh}$ is determined predominantly by the shearing of γ'' precipitates. Variations of the measured σ_y are plotted in Fig. 15 for the 4 cross sections with ≥70 wt% IN718. In the same plot, variations of the calculated σ_y, by considering the individual contributions of $\Delta\sigma_{sh}$ and $\Delta\sigma_{oro}$ as the primary precipitate strengthening mechanism, are superimposed for comparison. $\Delta\sigma_{sh}$ and $\Delta\sigma_{oro}$ are calculated by substituting values of values of r, L which are listed in Table 3, in eq. (6) and eqs. (7), (8), (9). Note that, in each case,

only σ0, $\Delta\sigma_{HP}$, and $\Delta\sigma_{DS}$ are considered for calculating σ_y whereas the strengthening contribution from $\Delta\sigma_{SS}$ is ignored. For the cross sections with ~70 and 80 wt% IN718, σ_y, calculated by considering the Orowan bypass mechanism as the operating precipitate strengthening mechanism, matches closely with the measured σ_y.
Alternately, σ_y calculated by considering the precipitate shearing mechanism is a closer match with the experimental data for cross sections with ~90 and 100 wt% IN718.

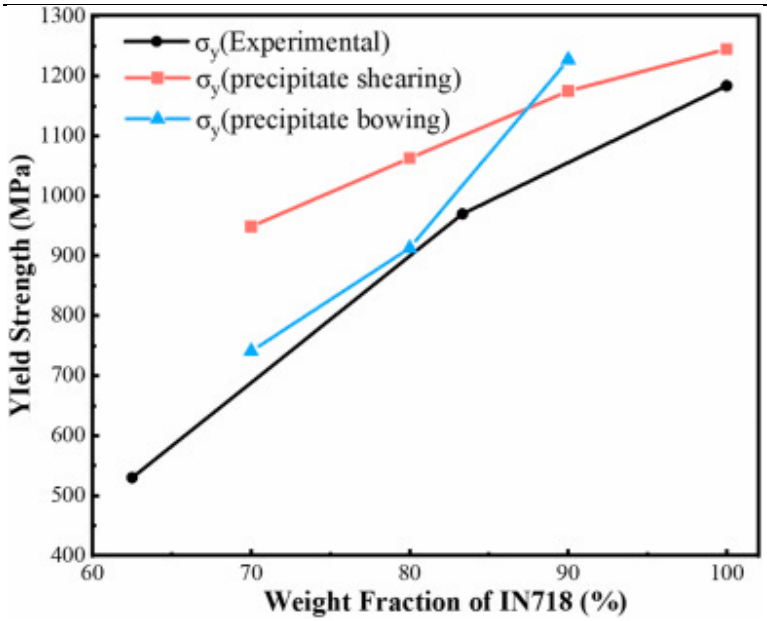

1. Download: Download high-res image (260KB)
2. Download: Download full-size image

Fig. 15. Measured and calculated σ_y of heat-treated CGA for cross sections with ≥70 wt% IN718 along GD.

Preference for the Orowan bypass mechanism in cross sections with ~70 and 80 wt% IN718 is attributed to their higher Λ of the precipitates in them. A higher Λ, which signifies greater spacing between the dislocation pinning precipitates, allows dislocations to escape at a lower applied stress. In contrast, for precipitates with lower Λ, as in the case of cross sections with ~90 and 100 wt% IN718, the pinned dislocations need higher stress to bow outward compared to the stress required to shear precipitates. However, it is imperative to treat this analysis as semi-quantitative as the contributions from ΔσSS were considered, owing to our inability to measure the exact composition of the matrix after heat treatment.

4.2.3. Post yield deformation in as-built and heat-treated SS316L/IN718 CGA

Post yielding, all cross sections of the as-built and heat-treated CGA exhibit varying degrees of strain hardening. The degree of strain hardening, characterized by *n*, is primarily the outcome of resistance to dislocation slip due to interactions with other dislocations and to a lesser extent by obstacles such as precipitates or grain boundaries.

Typically, plastic deformation itself creates new dislocations and promotes cross slip of existing dislocations onto different intersecting slip planes, which act as obstacles and hinder the motion of existing dislocations, which in turn, promotes strain hardening. However, if the dislocation content in the material is already considerably high, the ability of the material to strain harden saturates and dynamic recovery, involving annihilation of dislocations, gets initiated. The lower n of all the cross sections in the as-built CGA compared to their heat-treated counterparts is an outcome of this hardening saturation (see Table 4, Table 5). Note that the contraction strain developed in the CGA during LPBF is accommodated by a large density of dislocations networks, which manifest as sub-grains or cellular structures within grains (see Fig. 4 and S1). In contrast, the heat-treated CGA has a lower density of dislocations, indicated by the disappearance of the cellular structures within grains and lower GND estimated from EBSD images (see Fig. 4, Table 6 and S1). On account of higher initial dislocation densities in the cross sections of the as-built CGA, dynamic recovery will initiate at relatively lower strains, compared to that in its heat-treated counterpart. This leads to lower extent of strain hardening in the former than that in the latter.

Note that strain hardening homogenizes plastic flow in the material as it promotes transmission of slip to different planes and mitigates strain localization. The good match between n and ε_u in most cross sections of the as-built CGA (see Fig. 4, Fig. 5) confirms that they initially undergo homogeneous plastic deformation. However, in these cross sections, straining beyond ε_u leads to the onset of strain localization, which in turn causes instant failure. For the cross section with 25 wt%, $\varepsilon_u < n$, suggesting that it failed prematurely.

Similarly, all cross sections of the heat-treated CGA also fail before $\varepsilon_u \sim n$. Premature failure of these cross sections during homogeneous plastic flow is attributed to elevated contents of Laves phases in them (see Fig. 13 and S4), which are inherently brittle. In fact, in cross sections with 0 and 8 wt% IN718 of the heat-treated CGA, which have lower volume fraction of Laves phases, fail after $\varepsilon_u \sim n$. Embrittlement of Ni based superalloys and steels due to the presence of Laves phases has also been reported in previous studies and identified as one of the key problems affecting their performance in service [32].

4.2.4. Other considerations

From the preceding discussions, it is evident that only certain combinations of SS316L and IN718 possess favorable mechanical properties. While the overall strength of the CGA with the addition of IN718 is broadly higher than that of pure SS316L, some combinations such as one with ~ 25 wt% IN718 possess low strength and ductility. Therefore, a SS316L/IN718 CGA with >25 wt% IN718 is preferred. Moreover, in the as-built condition of such a CGA, the increase in strength from the SS316L rich end to the IN718 rich end is only incremental. In contrast, the DA heat treatment increases the strength significantly in the end with >70 wt% IN718, due to the precipitation of γ" and γ' phases. However, this strengthening of the portion with >70 wt% IN718 comes at the cost of deterioration of overall deformability and toughness owing to the increased precipitation and coarsening of Laves phases during heat treatment. Therefore, the

design and heat treatment of SS316L/IN718 CGA for structural applications requires careful scrutiny of these mechanical property trade-offs.

5. Summary and conclusions

A customized LPBF process, which creates compositional gradient along the powder bed plane, is employed for fabricating a highly dense CGA of SS316L and IN718. This CGA is subjected to a standard double ageing heat treatment used for strengthening IN718. The microstructural and mechanical properties of the CGA in the as-built and heat-treated condition were characterized. Following are the key findings of this study:

1) Process optimization, with the aim of obtaining a part with relative density >99%, also ensures intimate mixing of SS316L and IN718, which is he likely cause for smooth composition variations from the SS316L-rich end to the IN718-rich end.
2) The microstructure in every cross section of the as-built CGA along the GD, irrespective of the composition, consists of micron sized <001> textured columnar grains of the FCC γ phase, within which sub-micron sized cells are observed. While varying contents of Laves phases are present in broadly all cross sections of the CGA, their volume fraction does not exceed ~ 2%.
3) The double ageing heat treatment annihilates the cell structure, modifies the texture significantly, and increases the size and volume fraction of the Laves phases but does not lead to grain coarsening. Also, precipitation of γ" and γ' phases is observed, but only in the portion of the CGA with >70 wt% IN718.
4) The H, YS and UTS of the as-built CGA increases but ductility decreases from the SS316L-rich end to the IN718-rich end. A significant departure from these trends in these properties is observed at the cross section with 25 wt% IN718, which exhibits brittleness due to the higher volume fraction of Laves phases in it. However, a good match between ductility and strain hardening exponent confirms that the CGA undergoes uniform deformation before undergoing failure.
5) In the heat-treated CGA, the YS and UTS of the portions of the built with <82 wt% IN718 is lower than that in the as-built condition. Alternately, the reduced dislocation density in all cross sections of the CGA after heat treatment enhances strain hardening rate. However, this does not improve the ductility as the coarsened Laves phases in these cross sections lead to premature failure.
6) YS and UTS of the heat-treated CGA in portions with >82 wt% IN718 is significantly higher than that in the as-built condition owing to the precipitate strengthening by the γ" and γ' precipitates. However, the presence of Laves phases significantly deteriorates its ductility.
7) Results indicate that the portions of the CGA where the content of IN718 exceeds 25 wt% is suitable for structural applications. The double ageing heat treatment appears to be unsuitable for enhancing mechanical properties as it does not improve the strength of the SS316L-rich portions of the CGA and also leads to the embrittlement of IN718-rich end.

CRediT authorship contribution statement

Yaojie Wen: Methodology, Investigation, Writing – original draft. **Jianbao Gao:** Software, Data curation. **Ramasubramanian Lakshmi Narayan:** Investigation, Writing – review editing. **Pei Wang:** Software,

Validation. **Lijun Zhang:** Supervision. **Baicheng Zhang:** Conceptualization, Writing – review editing. **Upadrasta Ramamurty:** Supervision. **Xuanhui Qu:** Supervision.

Declaration of competing interest

The authors declare that they have no known competing financial interests or personal relationships that could have appeared to influence the work reported in this paper.

Acknowledgement

The authors acknowledge the financial support of the National Key R&D Program of China (2021YFB38002300), National Natural Science Foundation of China (No.: 52171026, 51901020). RLN's research at IITD was supported through the Start-up research grant (No. SRG/2020/000095) of Science and Engineering Research Board, DST, GoI. Research at NTU was supported by the Structural Metal Alloys Program (Grant Ref. No. A18b1B0061) of the Agency for Science, Technology and Research of Singapore. Research at IMRE was supported by the AME (IRG) Thematic Grant Call on Cleaner Manufacturing, grant No. A20E7c0109, in Agency for Science, Technology and Research in Singapore.

Appendix A. Supplementary data

The following is the Supplementary data to this article:

Download: Download Word document (14MB)

Multimedia component 1.

Data availability

Data will be made available on request.

References

[1]

S.J. Zinkle, G.S. Was

Materials challenges in nuclear energy

Acta Mater., 61 (2013), pp. 735-758, 10.1016/J.ACTAMAT.2012.11.004
View PDFView articleView in ScopusGoogle Scholar

[2]

C.R.F. Azevedo

Selection of fuel cladding material for nuclear fission reactors

Eng. Fail. Anal., 18 (2011),
p. 1943, 10.1016/J.ENGFAILANAL.2011.06.010
–1962
View PDFView articleView in ScopusGoogle Scholar
[3]

M.B. Henderson, D. Arrell, R. Larsson, M. Heobel, G. Marchant, Science and Technology of Welding and Joining Nickel based superalloy welding practices for industrial gas turbine applications Nickel based superalloy welding practices for industrial gas turbine applications,
(n.d.). https://doi.org/10.1179/136217104225017099.
Google Scholar
[4]

J.L. Robinson, M. Scott

Liquation cracking during the welding of austenitic stainless steels and nickel alloys

Philos. Trans. R. Soc. London. Ser. A, Math. Phys. Sci., 295 (1980),
pp. 105-117, 10.1098/RSTA.1980.0079
Google Scholar
[5]

B. Zhang, M. Xiu, Y.T. Tan, J. Wei, P. Wang

Pitting corrosion of SLM Inconel 718 sample under surface and heat treatments

Appl. Surf. Sci., 490 (2019), pp. 556-567, 10.1016/j.apsusc.2019.06.043
View PDFView articleView in ScopusGoogle Scholar
[6]

K. Shah, I. ul Haq, A. Khan, S.A. Shah, M. Khan, A.J. Pinkerton

Parametric study of development of Inconel-steel functionally graded materials by laser direct metal deposition

Mater. Des., 54 (2014), pp. 531-538, 10.1016/J.MATDES.2013.08.079
View PDFView articleView in ScopusGoogle Scholar
[7]

Y.F. Li, S.T. Hong, H. Choi, H.N. Han

Solid-state dissimilar joining of stainless steel 316L and Inconel 718 alloys by electrically assisted pressure joining

Mater. Char., 154 (2019), pp. 161-168, 10.1016/j.matchar.2019.06.005
View PDFView articleGoogle Scholar
[8]

B. Binesh

Diffusion brazing of IN718/AISI 316L dissimilar joint: microstructure evolution and mechanical properties

J. Manuf. Process., 57 (2020), pp. 196-208, 10.1016/j.jmapro.2020.06.025
View PDFView articleView in ScopusGoogle Scholar
[9]

M.J. Paul, Q. Liu, J.P. Best, X. Li, J.J. Kruzic, U. Ramamurty, B. Gludovatz

Fracture resistance of $AlSi_{10}Mg$ fabricated by laser powder bed fusion
Acta Mater., 211 (2021),
Article 116869, 10.1016/J.ACTAMAT.2021.116869
View PDFView articleView in ScopusGoogle Scholar
[10]

P. Kumar, U. Ramamurty

High cycle fatigue in selective laser melted Ti-6Al-4V

Acta Mater., 194 (2020), pp. 305-320, 10.1016/J.ACTAMAT.2020.05.041
View PDFView articleView in ScopusGoogle Scholar
[11]

S. Wei, K.B. Lau, J.J. Lee, F. Wei, W.H. Teh, B. Zhang, C.C. Tan, P. Wan g, U. Ramamurty

Selective laser melting of Fe–Al alloys with simultaneous gradients in composition and microstructure

Mater. Sci. Eng. A, 821 (2021),
Article 141608, 10.1016/J.MSEA.2021.141608
View PDFView articleView in ScopusGoogle Scholar
[12]

P. Kumar, R. Jayaraj, J. Suryawanshi, U.R. Satwik, J. McKinnell, U. Rama murty

Fatigue strength of additively manufactured 316L austenitic stainless steel

Acta Mater., 199 (2020), pp. 225-239, 10.1016/j.actamat.2020.08.033
View PDFView articleGoogle Scholar
[13]

X. Mei, X. Wang, Y. Peng, H. Gu, G. Zhong, S. Yang

Interfacial characterization and mechanical properties of 316L stainless steel/inconel 718 manufactured by selective laser melting

Mater. Sci. Eng. A., 758 (2019), pp. 185-191, 10.1016/j.msea.2019.05.011
View PDFView articleView in ScopusGoogle Scholar
[14]

S.H. Kim, H. Lee, S.M. Yeon, C. Aranas, K. Choi, J. Yoon, S.W. Yang, H. Lee

Selective compositional range exclusion via directed energy deposition to produce a defect-free Inconel 718/SS 316L functionally graded material

Addit. Manuf., 47 (2021), Article 102288, 10.1016/j.addma.2021.102288
View PDFView articleView in ScopusGoogle Scholar
[15]

D. Melzer, J. Džugan, M. Koukolíková, S. Rzepa, J. Vavřík

Structural integrity and mechanical properties of the functionally graded material based on 316L/IN718 processed by DED technology

Mater. Sci. Eng. A., 811 (2021), 10.1016/j.msea.2021.141038
Google Scholar
[16]

W.Y. Chen, X. Zhang, M. Li, R. Xu, C. Zhao, T. Sun

Laser powder bed fusion of Inconel 718 on 316 stainless steel

Addit. Manuf., 36 (2020), Article 101500, 10.1016/j.addma.2020.101500
View PDFView articleView in ScopusGoogle Scholar

[17]

Y. Su, B. Chen, C. Tan, X. Song, J. Feng

Influence of composition gradient variation on the microstructure and mechanical properties of 316 L/Inconel718 functionally graded material fabricated by laser additive manufacturing

J. Mater. Process. Technol., 283 (2020), 10.1016/j.jmatprotec.2020.116702
Google Scholar
[18]

X. Liang, D. Wu, Q. Li, L. Jiang

Laser rapid manufacturing of stainless steel 316L/Inconel718 functionally graded materials: microstructure evolution and mechanical properties

Int. J. Opt., 2010 (2010), pp. 1-6, 10.1155/2010/802385
View in ScopusGoogle Scholar
[19]

S. Mohd Yusuf, X. Zhao, S. Yang, N. Gao

Interfacial characterisation of multi-material 316L stainless steel/Inconel 718 fabricated by laser powder bed fusion

Mater. Lett., 284 (2021), Article 128928, 10.1016/j.matlet.2020.128928
View PDFView articleView in ScopusGoogle Scholar
[20]

K. Li, J. Zhan, M. Zhang, R. Ma, Q. Tang, D.Z. Zhang, L.E. Murr, H. Cao

A functionally graded material design from stainless steel to Ni-based superalloy by laser metal deposition coupled with thermodynamic prediction

Mater. Des., 217 (2022), Article 110612, 10.1016/J.MATDES.2022.110612
View PDFView articleView in ScopusGoogle Scholar
[21]

Y. Wen, B. Zhang, R.L. Narayan, P. Wang, X. Song, H. Zhao, U. Ramamurty, X. Qu

Laser powder bed fusion of compositionally graded CoCrMo-Inconel 718

Addit. Manuf., 40 (2021), Article 101926, 10.1016/j.addma.2021.101926
View PDFView articleView in ScopusGoogle Scholar
[22]

ASTM International

E3 preparation of metallographic specimens

Annu. Book ASTM Stand., 11 (2017), pp. 1-17, 10.1520/E0003-11R17.1
Google Scholar
[23]

J.-O. Andersson, T. Helander, L. Höglund, P. Shi, B. Sundman

Thermo-Calc & DICTRA, computational tools for materials science

Calphad, 26 (2002), pp. 273-312

View PDFView articleView in ScopusGoogle Scholar
[24]

Thermo-Calc Software and Databases (2015)

Google Scholar
[25]

J. Gao, J. Zhong, G. Liu, S. Yang, B. Song, L. Zhang, Z. Liu

A machine learning accelerated distributed task management system (Malac-Distmas) and its application in high-throughput CALPHAD computations aiming at efficient alloy design

Adv. Powder Mater. (2021), 10.1016/j.apmate.2021.09.005
Google Scholar
[26]

B.E. Carroll, R.A. Otis, J.P. Borgonia, J. Suh, R.P. Dillon, A.A. Shapiro, D. C. Hofmann, Z.-K. Liu, A.M. Beese

Functionally graded material of 304L stainless steel and inconel 625 fabricated by directed energy deposition: characterization and thermodynamic modeling

Acta Mater., 108 (2016), pp. 46-54, 10.1016/j.actamat.2016.02.019
View PDFView articleView in ScopusGoogle Scholar
[27]

K.G. Prashanth, J. Eckert

Formation of metastable cellular microstructures in selective laser melted alloys

J. Alloys Compd., 707 (2017), pp. 27-34

View PDFView articleView in ScopusGoogle Scholar
[28]

D. Deng, R.L. Peng, H. Brodin, J. Moverare

Microstructure and mechanical properties of Inconel 718 produced by selective laser melting: sample orientation dependence and effects of post heat treatments

Mater. Sci. Eng. A., 713 (2018), pp. 294-306, 10.1016/j.msea.2017.12.043
View PDFView articleView in ScopusGoogle Scholar
[29]

S. Gao, Z. Hu, M. Duchamp, P.S.S.R. Krishnan, S. Tekumalla, X. Song, M . Seita

Recrystallization-based grain boundary engineering of 316L stainless steel produced via selective laser melting

Acta Mater., 200 (2020), pp. 366-377, 10.1016/j.actamat.2020.09.015
View PDFView articleView in ScopusGoogle Scholar
[30]

S. Gorsse, C. Hutchinson, M. Gouné, R. Banerjee

Science and Technology of Advanced Materials Additive manufacturing of metals: a brief review of the characteristic microstructures and properties of steels, Ti-6Al-4V and high-entropy alloys

Sci. Technol. Adv. Mater., 18 (2017), pp. 584-610, 10.1080/14686996.2017.1361305
View in ScopusGoogle Scholar
[31]

S.H. Li, Y. Zhao, J. Radhakrishnan, U. Ramamurty

A micropillar compression investigation into the plastic flow properties of additively manufactured alloys

Acta Mater., 240 (2022),
Article 118290, 10.1016/J.ACTAMAT.2022.118290
View PDFView articleView in ScopusGoogle Scholar
[32]

S. Sui, H. Tan, J. Chen, C. Zhong, Z. Li, W. Fan, A. Gasser, W. Huang

The influence of Laves phases on the room temperature tensile properties of Inconel 718 fabricated by powder feeding laser additive manufacturing

Acta Mater., 164 (2019), pp. 413-427, 10.1016/j.actamat.2018.10.032
View PDFView articleView in ScopusGoogle Scholar
[33]

S.A. Mantri, S. Dasari, A. Sharma, T. Alam, M.V. Pantawane, M. Pole, S. Sharma, N.B. Dahotre, R. Banerjee, S. Banerjee

Effect of micro-segregation of alloying elements on the precipitation behaviour in laser surface engineered Alloy 718

Acta Mater., 210 (2021), Article 116844, 10.1016/j.actamat.2021.116844
View PDFView articleView in ScopusGoogle Scholar
[34]

K.N. Amato, S.M. Gaytan, L.E. Murr, E. Martinez, P.W. Shindo, J. Hernan dez, S. Collins, F. Medina

Microstructures and mechanical behavior of Inconel 718 fabricated by selective laser melting

Acta Mater., 60 (2012), pp. 2229-2239, 10.1016/j.actamat.2011.12.032
View PDFView articleView in ScopusGoogle Scholar
[35]

E. Chlebus, K. Gruber, B. Kuźnicka, J. Kurzac, T. Kurzynowski

Effect of heat treatment on the microstructure and mechanical properties of Inconel 718 processed by selective laser melting

Mater. Sci. Eng. A., 639 (2015), pp. 647-655, 10.1016/j.msea.2015.05.035
View PDFView articleView in ScopusGoogle Scholar
[36]

G.A. Rao, M. Kumar, M. Srinivas, D.S. Sarma

Effect of standard heat treatment on the microstructure and mechanical properties of hot isostatically pressed superalloy inconel 718

Mater. Sci. Eng. A., 355 (2003), pp. 114-125, 10.1016/S0921-5093(03)00079-0
View PDFView articleView in ScopusGoogle Scholar
[37]

F. Theska, K. Nomoto, F. Godor, B. Oberwinkler, A. Stanojevic, S.P. Ringer, S. Primig

On the early stages of precipitation during direct ageing of Alloy 718

Acta Mater., 188 (2020), pp. 492-503, 10.1016/j.actamat.2020.02.034
View PDFView articleView in ScopusGoogle Scholar
[38]

S. Zhang, X. Lin, L. Wang, X. Yu, Y. Hu, H. Yang, L. Lei, W. Huang

Strengthening mechanisms in selective laser-melted Inconel718 superalloy

Mater. Sci. Eng. A., 812 (2021),
Article 141145, 10.1016/j.msea.2021.141145
View PDFView articleView in ScopusGoogle Scholar
[39]

T.R. Smith, J.D. Sugar, C. San Marchi, J.M. Schoenung

Strengthening mechanisms in directed energy deposited austenitic stainless steel

Acta Mater., 164 (2019), pp. 728-740, 10.1016/j.actamat.2018.11.021
View PDFView articleView in ScopusGoogle Scholar
[40]

D.M. Dimiduk, M.D. Uchic, T.A. Parthasarathy

Size-affected single-slip behavior of pure nickel microcrystals

Acta Mater., 53 (2005), pp. 4065-4077

View PDFView articleView in ScopusGoogle Scholar

[41]

E.O. Hall

The deformation and ageing of mild steel: III discussion of results

Proc. Phys. Soc. Sect. B., 64 (1951), p. 747, 10.1088/0370-1301/64/9/303
Google Scholar
[42]

Y.M. Wang, T. Voisin, J.T. McKeown, J. Ye, N.P. Calta, Z. Li, Z. Zeng, Y. Zhang, W. Chen, T.T. Roehling, R.T. Ott, M.K. Santala, P.J. Depond, M.J. Matthews, A.V. Hamza, T. Zhu

Additively manufactured hierarchical stainless steels with high strength and ductility

2017

Nat. Mater., 171 (17) (2017), pp. 63-71, 10.1038/nmat5021
View in ScopusGoogle Scholar
[43]

F. Wallow, E. Nembach

Synergisms of grain boundary and γ′-particle strengthening in nickel-base superalloys

Scripta Mater., 34 (1996), pp. 499-505, 10.1016/S0956-716X(95)00548-A
View PDFView articleView in ScopusGoogle Scholar
[44]

Y. Zhong, L. Liu, S. Wikman, D. Cui, Z. Shen

Intragranular cellular segregation network structure strengthening 316L stainless steel prepared by selective laser melting

J. Nucl. Mater., 470 (2016), pp. 170-178, 10.1016/J.JNUCMAT.2015.12.034
View PDFView articleView in ScopusGoogle Scholar
[45]

X. Wang, J.A. Muñiz-Lerma, O. Sánchez-Mata, M. Attarian Shandiz, M. Brochu

Microstructure and mechanical properties of stainless steel 316L vertical struts manufactured by laser powder bed fusion process

Mater. Sci. Eng. A., 736 (2018), pp. 27-40, 10.1016/J.MSEA.2018.08.069
View PDFView articleGoogle Scholar
[46]

L. Liu, Q. Ding, Y. Zhong, J. Zou, J. Wu, Y.L. Chiu, J. Li, Z. Zhang, Q. Yu, Z. Shen

Dislocation network in additive manufactured steel breaks strength–ductility trade-off

Mater. Today, 21 (2018), pp. 354-361, 10.1016/J.MATTOD.2017.11.004
View PDFView articleView in ScopusGoogle Scholar
[47]

T.H. Courtney

Mechanical Behavior of Materials

Waveland Press (2005)

Google Scholar
[48]

Y. Zhao, K.B. Lau, W.H. Teh, J.J. Lee, F. Wei, M. Lin, P. Wang, C.C. Tan, U. Ramamurty

Compositionally graded CoCrFeNiTix high-entropy alloys manufactured by laser powder bed fusion: a combinatorial assessment

J. Alloys Compd., 883 (2021), 10.1016/j.jallcom.2021.160825
Google Scholar
[49]

F. Wei, S. Wei, K.B. Lau, W.H. Teh, J.J. Lee, H.L. Seng, C.C. Tan, P. Wa ng, U. Ramamurty

Compositionally graded AlxCoCrFeNi high-entropy alloy manufactured by laser powder bed fusion

Materialia, 21 (2022), Article 101308, 10.1016/J.MTLA.2021.101308
View PDFView articleView in ScopusGoogle Scholar
[50]

H.J. Kong, C. Xu, C.C. Bu, C. Da, J.H. Luan, Z.B. Jiao, G. Chen, C.T. Liu

Hardening mechanisms and impact toughening of a high-strength steel containing low Ni and Cu additions

Acta Mater., 172 (2019), pp. 150-160, 10.1016/j.actamat.2019.04.041
View PDFView articleView in ScopusGoogle Scholar
[51]

H. Wen, T.D. Topping, D. Isheim, D.N. Seidman, E.J. Lavernia

Strengthening mechanisms in a high-strength bulk nanostructured Cu-Zn-Al alloy processed via cryomilling and spark plasma sintering

Acta Mater., 61 (2013), pp. 2769-2782, 10.1016/j.actamat.2012.09.036
View PDFView articleView in ScopusGoogle Scholar
[52]

T.H. Becker, U. Ramamurty

Fracture and fatigue in additively manufactured metals

Acta Mater., 219 (2021),
Article 117240, 10.1016/J.ACTAMAT.2021.117240
View PDFView articleView in ScopusGoogle Scholar
[53]

E.I. Galindo-Nava, L.D. Connor, C.M.F. Rae

On the prediction of the yield stress of unimodal and multimodal γ' Nickel-base superalloys

Acta Mater., 98 (2015), pp. 377-390, 10.1016/j.actamat.2015.07.048
View PDFView articleView in ScopusGoogle Scholar
[54]

L.A. Gypen, A. Deruyttere

Multi-component solid solution hardening - Part 2 Agreement with experimental results

J. Mater. Sci., 12 (1977), pp. 1034-1038, 10.1007/BF00540988
View in ScopusGoogle Scholar
[55]

L.A. Gypen, A. Deruyttere

Multi-component solid solution hardening - Part 1 Proposed model

J. Mater. Sci., 12 (1977), pp. 1028-1033, 10.1007/BF00540987
View in ScopusGoogle Scholar
[56]

H.A. Roth, C.L. Davis, R.C. Thomson

Modeling solid solution strengthening in nickel alloys

Metall. Mater. Trans. A Phys. Metall. Mater. Sci., 28 (1997), pp. 1329-1335, 10.1007/s11661-997-0268-2
View in ScopusGoogle Scholar
[57]

K. Ma, H. Wen, T. Hu, T.D. Topping, D. Isheim, D.N. Seidman, E.J. Lavernia, J.M. Schoenung

Mechanical behavior and strengthening mechanisms in ultrafine grain precipitation-strengthened aluminum alloy

Acta Mater., 62 (2014), pp. 141-155, 10.1016/j.actamat.2013.09.042
View PDFView articleView in ScopusGoogle Scholar
[58]

J.M. Oblak, D.F. Paulonis, D.S. Duvall

Coherency strengthening in Ni base alloys hardened by DO22 γ′ precipitates

Metall. Trans. A, 5 (1974), pp. 143-153, 10.1007/BF02642938
View in ScopusGoogle Scholar